Mass modeling and search for transients with AstroSat-CZTI

A Thesis

submitted to
Indian Institute of Science Education and Research Pune
in partial fulfillment of the requirements for the
BS-MS Dual Degree Programme

by

Arvind B

Indian Institute of Science Education and Research Pune
Dr. Homi Bhabha Road,
Pashan, Pune 411008, INDIA.

April, 2018

Supervisor: **Dr. Varun Bhalerao**

Certificate

This is to certify that this dissertation entitled Mass modeling and search for transients with AstroSat-CZTI towards the partial fulfilment of the BS-MS dual degree programme at the Indian Institute of Science Education and Research, Pune represents study/work carried out by **Arvind B** at Indian Institute of Technology, Bombay, under the supervision of **Dr. Varun Bhalerao**, Assistant Professor, Department of Physics, Indian Institute of Technology, Bombay , during the academic year 2017-2018.

Dr. Varun Bhalerao

Committee:

Dr. Varun Bhalerao

Dr. Prasad Subramanian

This thesis is dedicated to my gurus and parents

Declaration

I hereby declare that the matter embodied in the report entitled Mass modeling and search for transients with AstroSat-CZTI are the results of the work carried out by me at the Department of Physics, Indian Institute of Technology, Bombay, under the supervision of **Dr. Varun Bhalerao** and the same has not been submitted elsewhere for any other degree.

Arvind·B

Arvind B

Acknowledgments

I take this opportunity to thank my supervisor, Dr. Varun Bhalerao, for guiding me throughout the thesis and helping me out in every problem I faced during this time. It has been a great learning experience working under him.
I thank all the member of the CZTI team for their valuable inputs and suggestions at many stages of this thesis. Aarthy E, from Physical Research Laboratory, Ahmadabad, has been vital in running all the simulations, in the PRL cluster, the products of which have used in this thesis.
I humbly express my gratitude to Erin Sheldon, developer of the python package, `esutil`, for implementing a method in the package for use in the hierarchical triangular mesh grid.
I also thank Sujay Mate and Atharva Patil, for help in understanding and implementing many codes used during the analysis of data.

Abstract

Astrophysical transients are short timescale events, usually lasting from a few seconds to a few hundred seconds, and are sometimes associated with cataclysmic events like death of a star or merger of compact objects. This thesis focuses on the search for and study of astrophysical transients with the Cadmium Zinc Telluride Imager (CZTI), on-board AstroSat. At energies higher than 100 keV, CZTI functions as an open detector and is sensitive to transients from all over the sky. This makes it a very sensitive detector for various classes of astrophysical transients: Gamma Ray Bursts (GRBs), and even X-ray counterparts to gravitational wave events. As an all-sky detector, CZTI can detect transients shining through the satellite body. The analysis, localisation, and interpretation of this data requires a complete understanding of the absorption, scattering, and reprocessing of the incident photons by various elements of the satellite. Such interactions are impossible to compute analytically in a photon starved regime, since many of them are non-deterministic. This warrants the need for a simulation. A simulated "mass model" of the satellite has been developed using the GEANT4 simulation package. The scope of this thesis is to enhance the mass model and use it for studying various transients detected by CZTI, and to place strong upper limits on others.

Contents

List of Figures

List of Tables

Chapter 1

Introduction

The universe acts in mysterious ways and unraveling these mysteries is the main goal of all scientific disciplines. From exotic objects in space to our own bodies, we see a myriad of different processes. The study of cosmic objects has been carried out in various bands of the electromagnetic spectrum. Some of these bands are accessible from the surface of the earth, like the optical and radio. But, radiation from a major portion of the spectrum is not accessible to us due to the opaque nature of the atmosphere of the earth for those wavelengths (refer Figure 1.1). To probe the universe in these inaccessible wavelengths, instruments are launched into space.

X-rays, our band of interest, lies in this blocked portion of the spectrum. So, X-ray instruments need to be onboard satellites. In high energy astrophysics, it is customary to use energy instead of wavelength/frequency for defining bands of the electromagnetic spectrum and the X-ray band is categorized broadly into two sub-bands, **soft**, ranging from 0.1 keV to 10 keV and **hard**, ranging from 10 keV to 100 keV (1 eV = 1.6 $\times 10^{-19}$ J). X-ray data, simply put, consists of four parameters recorded for each incident photon : two parameters for coordinates of the point on the detector where the photon strikes, the time of incidence and the energy of the photon.

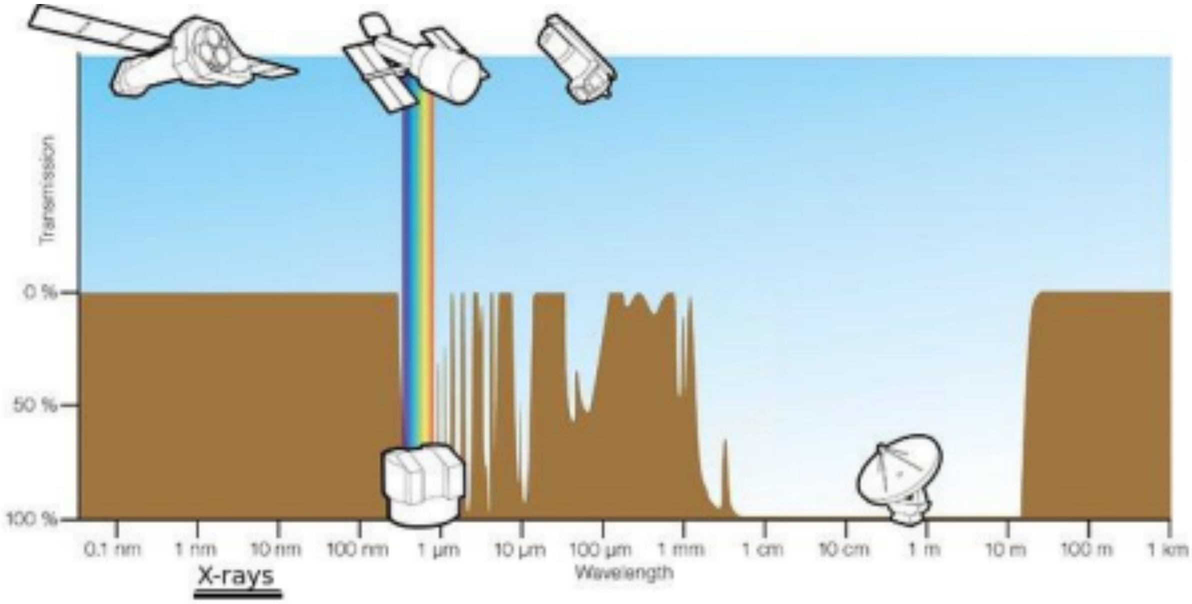

Figure 1.1: The atmospheric opacity as a function of wavelength. Notice that the X-ray band is in the portion of the electromagnetic spectrum blocked by the atmosphere. [1]

Processes like nuclear reactions and those involving physics of compact objects like black holes and neutron stars, are responsible for producing high energy electromagnetic radiation. Unlike other low energy radiation, observation techniques used in the detection of high energy radiation are very different due to the fact that it is not possible to converge these rays using lenses. The methods developed are of two types, one in which the rays are successively converged by making them incident at grazing angles on a large series of mirrors and another which uses a coded mask to image sources (dealt with in detail in Chapter 3.1).

This thesis aims at studying X-ray transients, some of the most fascinating objects owing to the large amounts of energy they release in a short span of time, using the Cadmium Zinc Telluride Imager hard X-ray instrument on AstroSat.

---

[1] Figure from `https://www.eso.org/public/usa/images/atm_opacity/`.

Chapter 2

Astrophysical transients

Astrophysical transients, henceforth referred to as transients, are events that occur at short time-scales, from a few seconds to a few months. Many a times, they are related to the death of a massive star, collision of compact objects etc. Let us look at some of the transients relevant to this thesis.

2.1 Gamma Ray Bursts (GRBs)

Gamma Ray Bursts (GRBs) were first discovered accidentally by detectors on the Vela spacecraft, built to look for sudden bursts of gamma rays emitted during nuclear tests. With the whole range of modern detectors at hand, we now observe about one such burst of gamma ray photons from a progenitor (source of a GRB), everyday. GRBs are classified into two broad categories [8]:

Short-hard GRBs :

- Last for at most 2 seconds.
- Alternatively called **hard** as a major portion of the gamma ray photons posses high energies.
- Progenitor is hypothesised to most probably be **neutron star-neutron star mergers**

(refer Chapter 5.2 on recent discoveries) or **neutron star-black hole mergers**.

Long-soft GRBs :

- Last for longer than 2s.
- **Soft** as majority of the emitted photons fall in lower energies.
- Thought to have **supernovae** origins.

The spectra of GRBs follow an empirical model called the **Band Model** [4]. According to the Band function, the photon number flux, $N(E)$ (photons cm^{-2} s^{-1} keV^{-1}), is given by a two power-law function.

$$N(E) = \begin{cases} A\left(\frac{E}{100}\right)^{\alpha} e^{\left(\frac{-E}{E_0}\right)} & \text{if } E \leq (\alpha-\beta)E_0 \\ A\left(\frac{(\alpha-\beta)E_0}{100}\right)^{(\alpha-\beta)} \left(\frac{E}{100}\right)^{\beta} e^{(\beta-\alpha)} & \text{if } E > (\alpha-\beta)E_0 \end{cases} \tag{2.1}$$

where E_0 is the energy at the peak in keV (where the powerlaw changes from one to the other) and α and β are the two powerlaw coefficients. A is a normalisation constant. The energy E is also in keV.

Energy flux is defined as the total amount of light energy passing through a unit surface perpendicular to its direction of propagation per unit time. The commonly used units for quantifying X-ray flux is ergs cm^{-2} s^{-1}. Another commonly used quantity is the **fluence**, which is the time integration of the energy flux over the duration of the burst. Fluence is expressed in ergs cm^{-2}. Energy flux for the GRB, given the photon flux $N(E)$, is therefore calculated as:

$$f(E) = \int_{E_{\min}}^{E_{\max}} N(E) * E dE \tag{2.2}$$

where, $E_{\min}$ and $E_{\max}$ are the limits over which the instrument is sensitive.

2.2 Electromagnetic counterparts of gravitational waves (EMGW)

One of Einstein's prediction in the general theory of relativity was that accelerating masses produce waves in space-time, that propagate at a speed equal the speed of light in vacuum. This new probe of the universe, other than the extensively used electromagnetic radiation, has come into the limelight in the past few years. In 2015, Laser Interferometric Gravitational-wave Observatory (LIGO) Consortium, announced its first confirmed detection of gravitational waves from the merger of two black holes [2] in a galaxy 1.3 billion light years away, nearly hundred years after the prediction by Einstein. Since then, we have had around six confirmed detections of other such mergers, the recent most one being the famous binary neutron star (BNS) merger (GW170817) on the 17th of August, 2017 [1]. What is so special about this observation is that, for the first time, scientists around the world have been able to observe the same source through electromagnetic counterparts as well [13]. The electromagnetic follow-up of gravitational wave observations is essential for many reasons :

- Locating the source. LIGO localisation patches are often very large, ~ 100 deg^2 to a few 1000 deg^2. Quick and effective localisation will enable other instruments to point at the sourceand extract all useful information.
- Identifying the compact objects that merged.
- Understanding the underlying physical principles of both the source and the emitted material.

2.2.1 Prompt emission

Short GRBs, as discussed above, are hypothesised to be associated with merger of binary neutron stars or a neutron star and a black hole. The emission mechanism of GRBs is known as prompt emission and the radiation is expected to be in the hard X-ray/gamma ray band. Some details of this mechanism are still not clear but a overall picture is well accepted. The composition of the GRB jet, its energy dissipation mechanism etc. are still unknown [19].

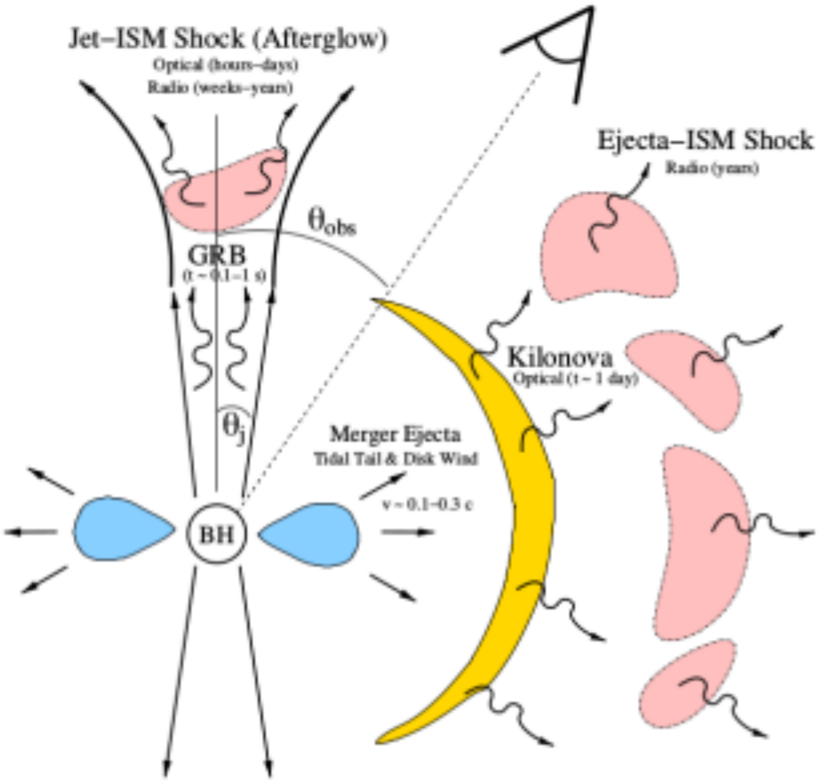

Figure 2.1: A figure showing possible counterparts from a BNS or a black hole neutron star merger. Figure used with permission from [14].

2.2.2 Kilonova

A binary neutron star or a neutron star black hole merger is accompanied by emission of light in almost all wavelength bands. This phenomenon is called **kilonova**. Kilonovae are theorised to be one of the main sources of elements heavier than Iron (Fe), apart from supernovae, including elements of even atomic numbers which are not found in remnants of supernovae. The process of emission of light from a kilonova is r-process nucleosynthesis. The recent multi-wavelength detections of the counterpart to GW170817, have confirmed the signature of heavy elements in the spectra of the merger remnant (for more details, refer [11]) .

Chapter 3

AstroSat - India's first observatory class space telescope

AstroSat, launched in 2015 by Indian Space Research Organisation (ISRO), is India's first astronomy satellite consisting of many coaxial instruments with an aim to obtain simultaneous data from sources in a wide band of the electromagnetic spectrum, ranging from hard X-rays to far UV [15]. Obtaining simultaneous data on sources in a wide range of wavelengths will help to get a holistic understand of the underlying physical principles of the source.

The science payloads onboard AstroSat are listed below [1]:

- LAXPC : Large Area X-ray Proportional Counters
- CZTI : Cadmium Zinc Telluride Imager
- SXT : Soft X-ray imaging Telescope
- SSM : Scanning Sky Monitor
- UVIT : Ultra Violet Imaging Telescope

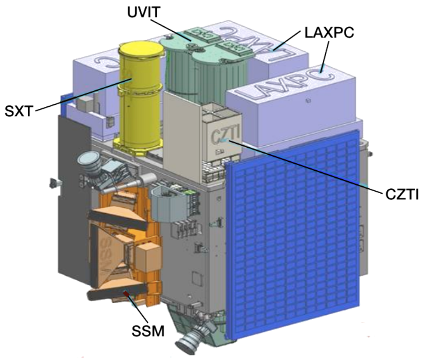

Figure 3.1: Payloads on AstroSat [1].

---

[1] http://astrosat.iucaa.in/

3.1 Cadmium Zinc Telluride Imager (CZTI)

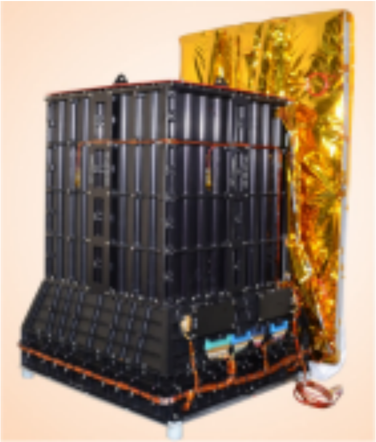

Figure 3.2: CZTI before integration on AstroSat [6].

Solid state detectors like silicon (Si) and germanium (Ge) cryogenic detectors are known for their excellent energy resolution. However, their low stopping potential for high energy photons cripples them when it comes to detection of hard X-rays and gamma rays. Cadmium Zinc Telluride is becoming an increasingly popular X-ray and gamma ray detector material due to the fact that it is a semiconductor with high atomic number (Z) - allowing it to absorb hard X-rays and that it has a wide band gap of 1.44 eV - making it usable as a detector in room temperature as well [17].

Cadmium Zinc Telluride Imager, CZTI (Figure 3.2), onboard AstroSat, is a wide-field instrument sensitive in the hard X-ray band (20 keV - 200 keV). It consists of sixty four Cadmium Zinc Telluride detector modules (each 5 mm thick $Cd_{0.9}Zn_{0.1}Te_{1.0}$ semiconductor crystals), manufactured by Orbotech Medical Solutions, Israel [2].

The primary science goals of the instrument are [6]:

- Spectral analysis of Active Galactic Nuclei and X-ray binary systems
- Study of Quasi-Periodic Oscillations at hard X-ray bands in accreting neutron star and black hole systems
- Spectra characterisation of hard X-ray spectra of magnetars
- Detection and lightcurve analysis of gamma ray bursts (GRBs)

---

[2] http://www.orbotech.com

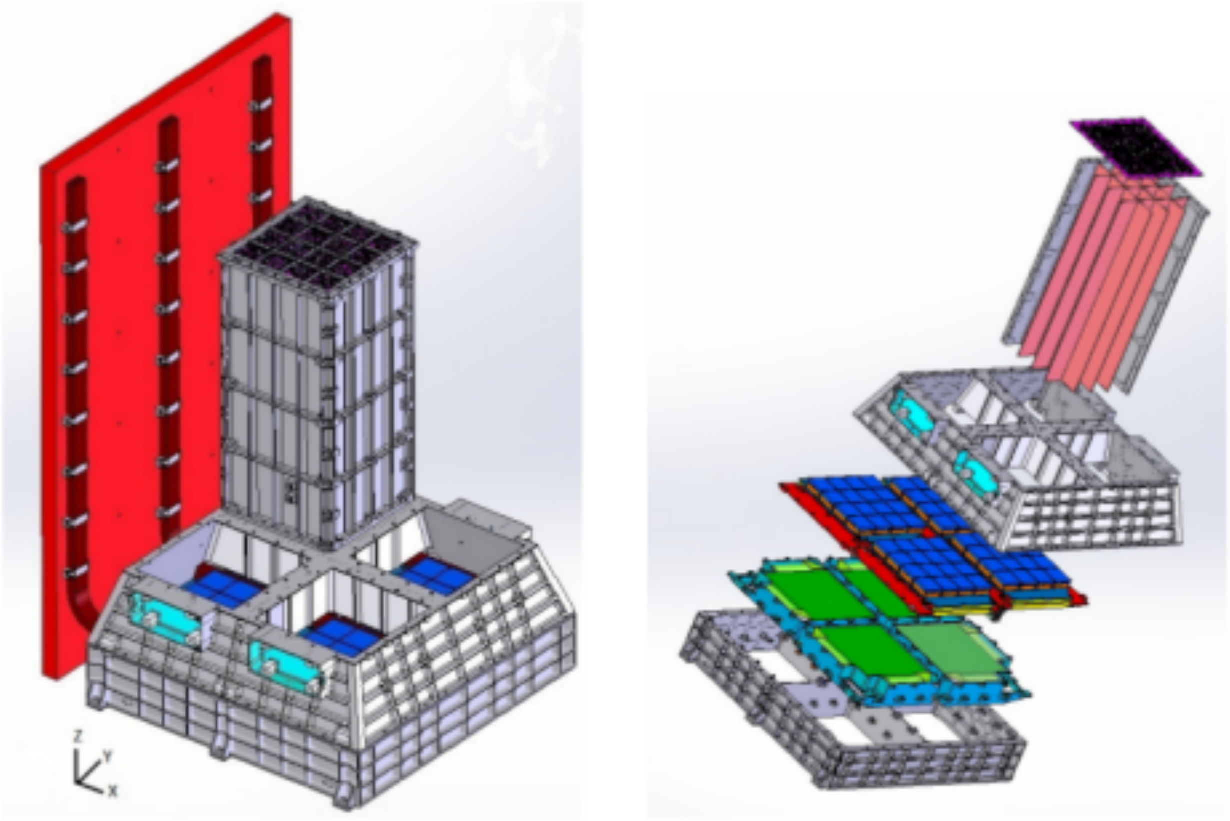

Figure 3.3: Layout of CZTI, adapted from [6].

The figure above gives the layout of the CZTI instrument. The bottom left corner contains the conventions used for the coordinate systems (discussed in the following section). In the left panel we see that the detector consists of four quadrants composed of sixteen CZT detector modules (blue) each. The radiator plate (red) is parallel to the z-axis and perpendicular to x-axis. The coded aperture mask is placed on top of the collimator housing (only one shown here for clarity). On the right, the components are separated out for ease of understanding. We, can spot from the top - the coded mask, the collimators, the detector modules, the veto detectors (green) used for differentiating X-ray photons from source of interest from cosmic rays and very high-energy photons and other calibrating devices.

Imaging X-ray sources is very different from other sources emitting in lower energies due to the inability to focus high energy radiation onto a detector, using lenses. CZTI makes use of a Coded Aperture Mask (CAM) (Figure 3.4 (a), for quadrant A only) to image sources.

CAM is a 0.5 mm thick Tantalum plate with a calculated pattern of rectangular apertures such that a unique shadow pattern is obtained on the detector for different directions of incident photons [7].

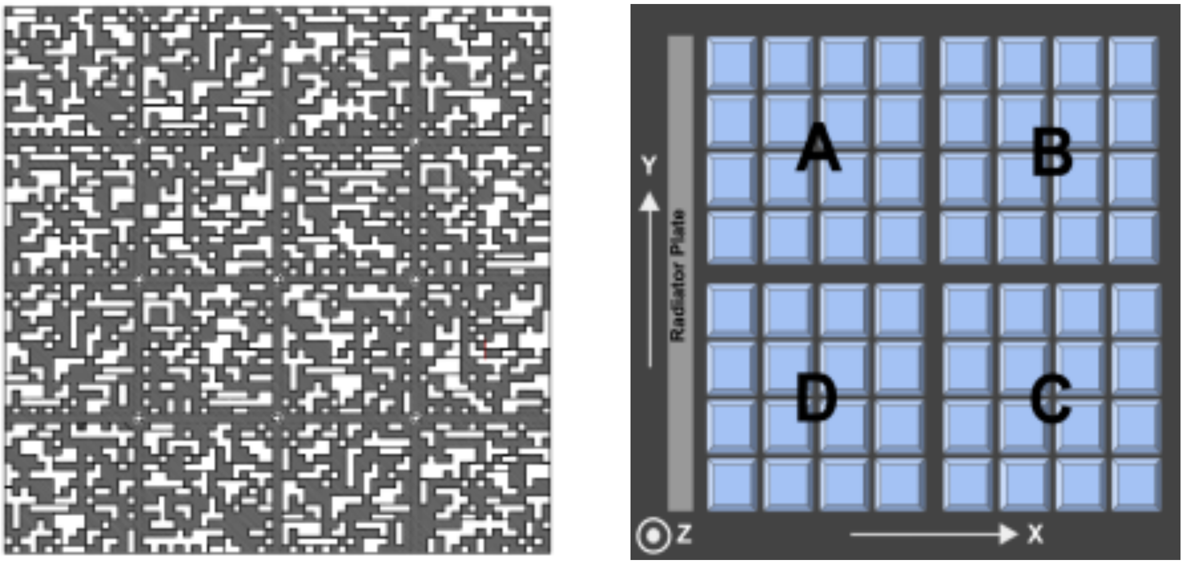

(a) (b)

Figure 3.4: *Left* : The Coded Aperture Mask (CAM) for quadrant A [6]. *Right* : A schematic representation showing the quadrants, A, B, C and D or 0, 1, 2 and 3 respectively, of CZTI (refer Figure 3.3 (left bottom) for the definition of the coordinate system).

The mask and collimator housing become transparent to photons above 100 keV. This in turn makes the instrument an open detector capable of all-sky detection and ideal for detecting off-axis (sources not in the field of view) transients like GRBs and counterparts to gravitational wave sources (refer Chapter 4).

3.1.1 Coordinate systems

The Figure 3.5 shows the coordinates of a transient, T (black) in two different commonly used conventions. A Cartesian system (refer Figure 3.3 left bottom corner and the figure below) is defined with the z-xis (red) parallel to the radiator plate facing up, x-axis (blue) perpendicular to the radiator plate towards the one of the LAXPC units and the y-axis (gray) towards the SXT and UVIT tubes. To locate any source on the sky we need two angles (the distance to the source is not of importance here). The system on the left uses direction cosines of T, obtained from projecting T onto the x-z and the y-z planes and measuring their angle from the z-axis to get θ_x and θ_y respectively. θ_x and θ_y, both range from -180^o to 180^o. The system on the right is more intuitive. In this system, the angle θ is the angle of the T from the z-axis and the angle ϕ is the angle between the x axis and the projection of T onto the x-y plane. θ ranges from 0^o to 180^o, while ϕ ranges from 0^o to 360^o.

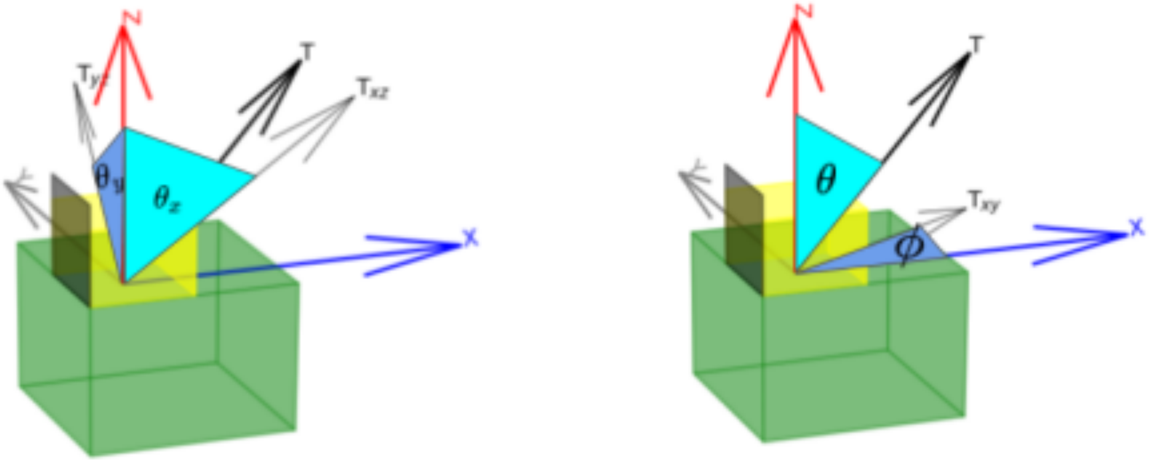

Figure 3.5: Illustrating the instrument coordinate system. The two panels above contain a cartoon of the satellite (yellow - CZTI collimators, gray - radiator plate, green - satellite body) and the coordinate axes marked in blue, gray and red (refer Figure 3.3). Assume T is some source. *Left* : Project the vector T onto x-z and y-z planes to get T_{xz} and T_{yz} respectively. θ_x is the angle between Z and T_{xz}, θ_y is the angle between Z and T_{yz}. *Right* : Project the vector T onto the x-y plane to get T_{xy}. θ is the angle between Z and T, ϕ is the angle between X and T_{xy}.

The $\theta_x - \theta_y$ system is good for on axis sources but has discontinuities on the detector plane (x-y plane) while the $\theta - \phi$ system has singularities at the poles.

Chapter 4

The need for mass model simulations

The interaction of radiation with matter is exploited in their detection. But some of these interactions may cause a change in the properties of the incident light. X-ray photons interact with matter through different mechanisms. Some such important interactions are described below (for more details refer [12]):

- **Mass attenuation/absorption :**
  X-rays of intensity I_0 are incident on a piece of a material, with thickness t and linear attenuation coefficient μ. The intensity of the emergent beam is given by :

  $$I = I_0 e^{-\mu t} \tag{4.1}$$

  Another quantity normally used is mass attenuation coefficient (μ/ρ) where ρ is the density of the material. The values of μ/ρ for various elements/materials have been experimentally determined and listed out. [1]

- **Photoelectric absorption :**
  When a photon is incident on an absorber atom, it is fully absorbed and the energy is transferred to one of the bound electrons (the ejected electron is called **photoelectron**). Mathematically, the energy of the ejected electron, E_{e^-}, is given in terms of the frequency, ν, of the incident photon and the binding energy E_b of the photoelectron in

---

[1] One such list is `https://www.nist.gov/pml/x-ray-mass-attenuation-coefficients`

its original shell :

$$E_{e^-} = h\nu - E_b \tag{4.2}$$

- **Compton scattering :**
  X-ray photons scatter off electrons of an atom to different lower energies. Henceforth, we will refer to this as **down-scattering**.

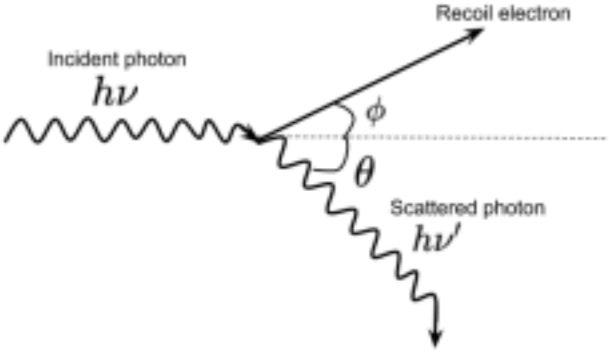

  The energy of the scattered photon is given by :

$$h\nu' = \frac{h\nu}{1 + \frac{h\nu}{m_0c^2}(1 - cos\theta)} \tag{4.3}$$

  where ν is the frequency of the incident photon, ν' is the frequency of the scattered photon, h is Planck's constant, m_0c^2 is the rest mass energy of the electron (0.511 MeV) and θ is the scattering angle of the photon.

- **Pair production :**
  For this process to be feasible, X-ray photon energies must be atleast two times the rest-mass energy of an electron (1.02 MeV). The photons disappear and leave an electron-positron pair.

- **Coherent scattering :**
  In these interactions, the photon retains its initial energy after the scattering and only changes its direction of propagation. The scatterer material is also unaffected. These processes are prominent for low energy photons and high atomic number substrates.

Sometimes, high energy photons just pass through a material without any interaction.

Figure 4.1 shows the relative importance of different processes for different energies of incident photons and for different atomic numbers of atoms making up the scatterer.

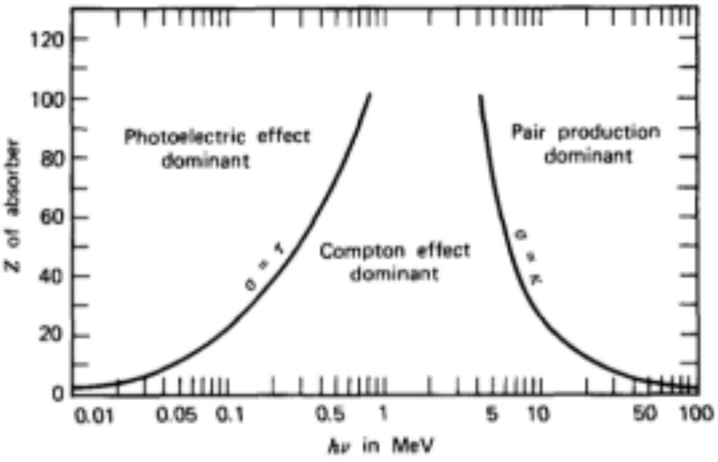

Figure 4.1: Relative importance of the three major types of X-ray interactions. The lines show the values Z (atomic number) and $h\nu$ (energy of incident photon) for which the two neighboring effects are just equal. Figure taken from [12] pg.52 .

Figure 4.2 shows the redistribution of incident photons to various energies by using a plot of the counts (directly related to the number of photons) detected in different energies for photons of 5 different incident energies (colour coded). We see that this redistribution, is so strong that even for incident photons with energies as high as 500 and 1000 keV (well outside the sensitivity range of CZTI which is 10 - 200 keV), we detect counts in energies as low as 100 keV (in the sensitivity range of CZTI).

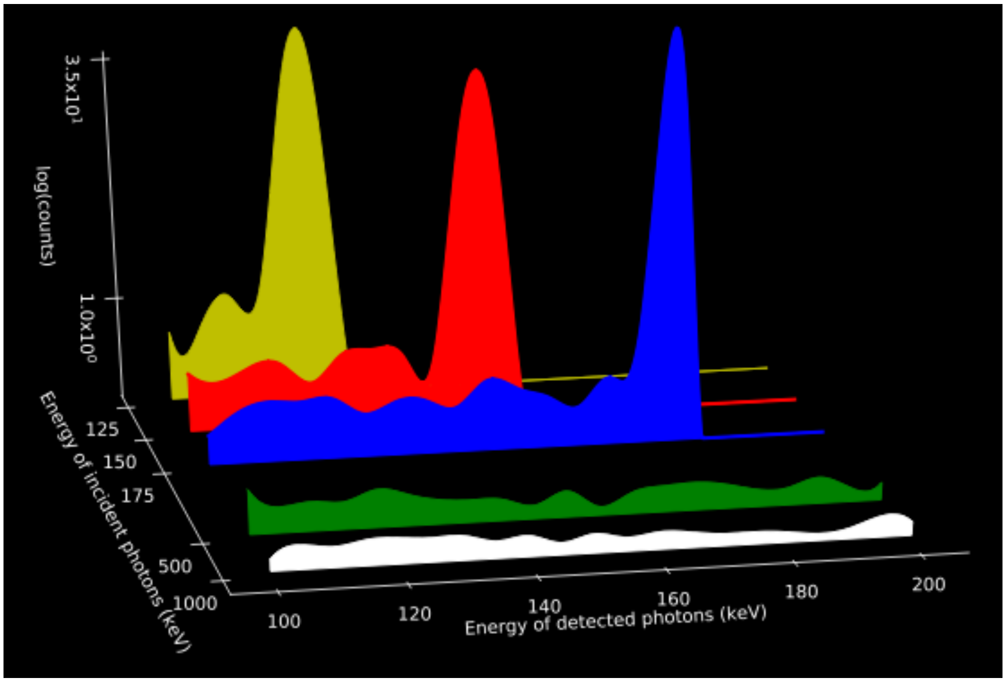

Figure 4.2: A graph showing the redistribution of incident photons from a simulated source to different energies.

Let us define an essential quantity which we will be referring to in the next few sections. **Effective area** is a measure of the sensitivity of a detector and it carries information on the interactions that the detected photons had, with other satellite elements. It can be defined as the area of an imaginary detector, oriented perpendicular to the direction of incidence of the photons, which will measure the same flux as the real detector. It is a function of both the direction of incidence of photons and the energy of the incident photons. A simple way to look at effective areas as a function of energy is shown in Figure 4.3. The absorbance of the detector, in general, will depend on the energy of the incident photons and hence will change the effective area in a non-trivial manner.

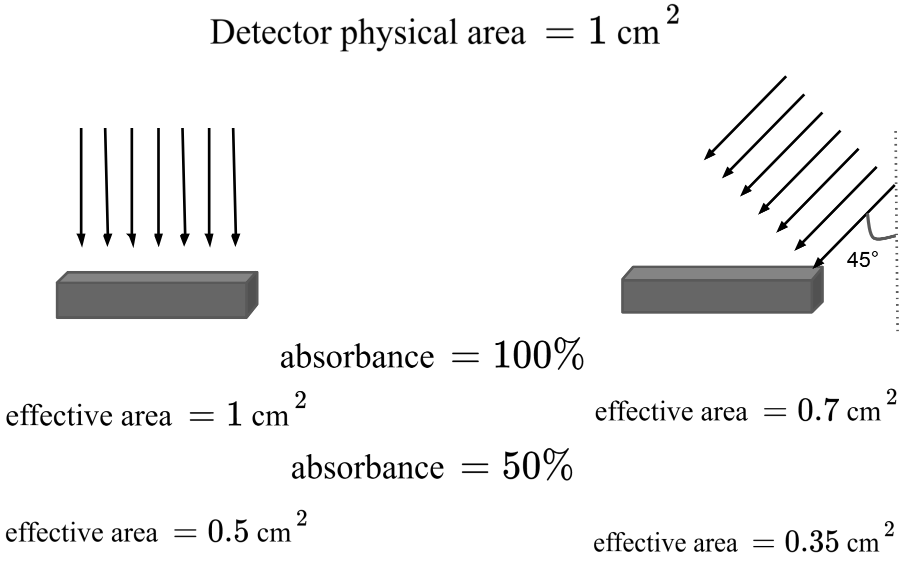

Figure 4.3: A cartoon showing the change in effective area a detector of physical area 1 cm^2 for different absorbances for the same energy of incident photons. For a real absorber, the absorbance, which is a function of energy of incident photons, will dictate the effective area. (Here, we are looking at the detector edge-on.)

Since we have already seen that CZTI starts to act as an open detector for photon energies above 100 keV, there is a possibility that the photons detected by the detector are reprocessed photons produced by some interaction with other satellite elements. Many of the above mentioned interactions (like Compton scattering) are non-deterministic and being in a **photon starved** X-ray regime, it is impossible to calculate interactions analytically. This warrants the need for simulations to understand these interactions better. The following section introduces simulations that have already been developed and discusses their pros and cons.

4.1 Raytrace simulation and its drawbacks

Raytrace is an analytical code which calculates the shadow (ie. the degree of absorption and transmission) cast by different components of CZTI on the detector, for photons of given energy and direction of incidence (refer Chapter 3.1.1) and then predicts the effective area for the same. There is one output file containing the effective areas for each pixel for that particular energy of the incident photons and their direction of incidence.

Listed below are the drawbacks of raytrace :

- Other satellite elements are not modeled.
- All interactions involving change in energy or direction of incident photons are not taken into account.
- Only top half of the hemisphere ($\theta < 90^o$, refer Chapter 3.1.1 for definition of θ) is modeled, but archived data contains many GRBs shining from below the detector plane ($90^o < \theta < 180^o$).

However, the raytrace products have been used successfully to simulate sources for which the interaction with other satellite elements is not that much profound and are still used for publishing upper limits (more discussion in Chapter 5.1). The following figure shows the effective area as a function of direction of incidence for photons different incident energy, calculated using raytrace products [6].

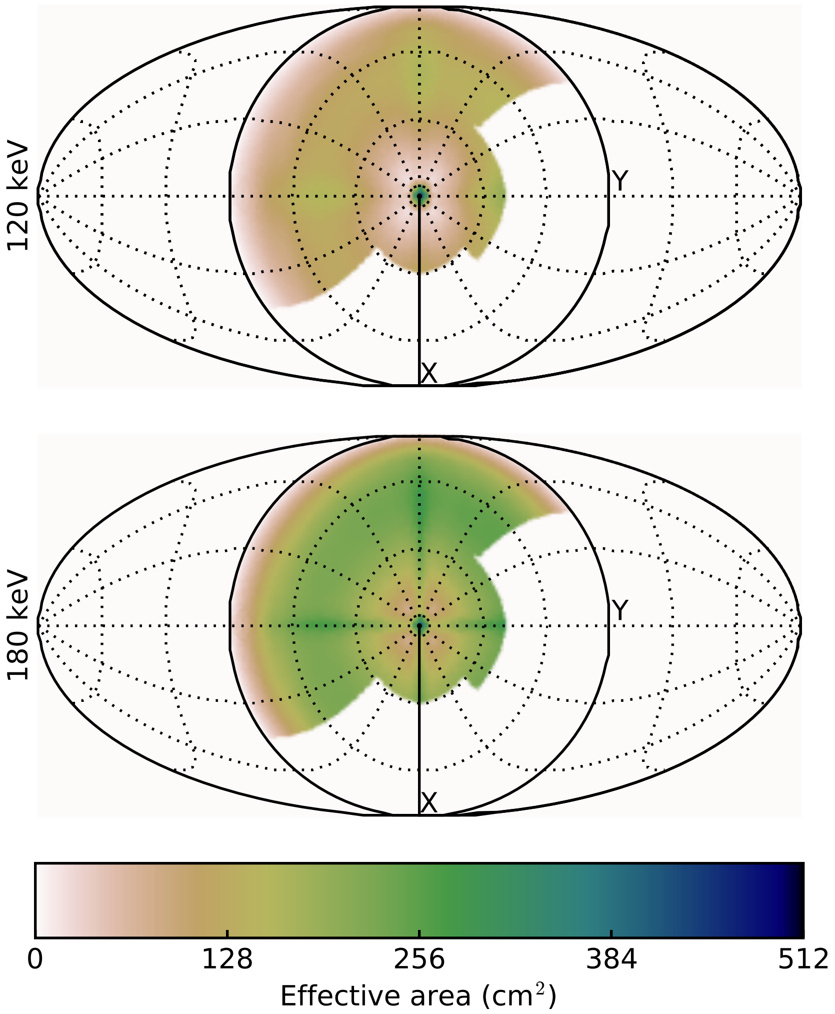

Figure 4.4: A Mollweide projection (a two dimensional projection of the whole sky) of the effective area as a function of direction of incidence for different incident energies . The x-axis points to the bottom of the page, y-axis to the right and the z-axis points out of the paper. Figure from [6].

Since these simulations do not take into account many of the interactions mentioned in this section above, they are very quick and can be run on a small laptop too. But, to model photon interactions with the satellite, we need a more extensive simulation taking into account all the relevant interactions.

4.2 Geant4 and the mass model

Geant4, is a software developed for simulating the interaction of particles with matter [9]. The software has inbuilt classes to define geometry of the system, particles involved in the interaction, physical processes of the interaction itself etc. The simulated model of AstroSat, referred to as mass model, has been designed using Geant4 classes. The entire satellite has been modeled to scale and with all materials carefully designed. The types of physical interactions of interest, of the photons with the satellite, have been custom defined to counter problems faced with ray-trace simulations (for instance, down-scattering is now accounted for).

The mass model was entirely designed before the beginning of this thesis project. A few modifications were made during the course of this thesis (refer to the section below).

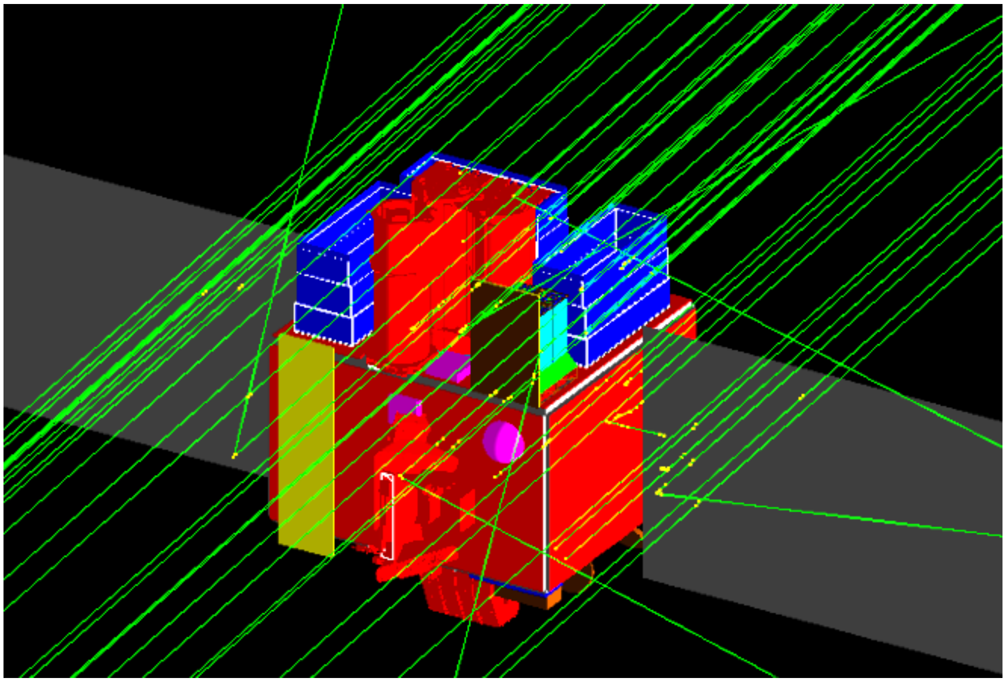

Figure 4.5: A GEANT4 rendered image of a simulation of a source shining 50 photons of one energy from a certain direction.

4.2.1 Modifications to the mass model

As we already saw, effective area for the detector is a function of both direction of incidence of photons and the energy of the photon. The mass model gives a unique output **fits** file(Flexible Image Transport System, a very effective format for storing images and binary tables [18]) for each energy and direction of incidence of the photons. The mass model was functioning properly before the modifications, but housekeeping was poor and the outputs occupied a large space in the storage. The modifications made by me during the course of this thesis has helped in making and streamlining the process of running large scale simulations possible, has added important metadata to headers of the output files and reduced the storage space required to store these outputs. The figure below shows the headers of the outputs before (left) and after (right) the modifications. Notice the useful metadata (energy of the incident photons, direction of incidence, seed used for the simulation etc.) present in the modified output header.

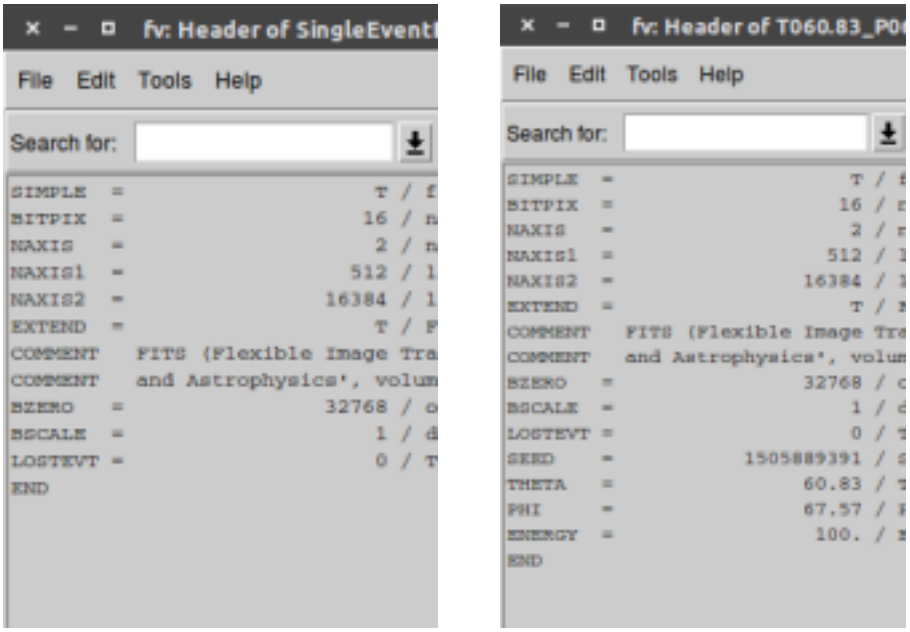

```
SIMPLE  =                    T / f
BITPIX  =                   16 / n
NAXIS   =                    2 / n
NAXIS1  =                  512 / 1
NAXIS2  =                16384 / 1
EXTEND  =                    T / F
COMMENT   FITS (Flexible Image Tra
COMMENT   and Astrophysics', volum
BZERO   =                32768 / o
BSCALE  =                    1 / d
LOSTEVT =                    0 / T
END
```

```
SIMPLE  =                    T / f
BITPIX  =                   16 / r
NAXIS   =                    2 / r
NAXIS1  =                  512 / 1
NAXIS2  =                16384 / 1
EXTEND  =                    T / F
COMMENT   FITS (Flexible Image Tra
COMMENT   and Astrophysics', volum
BZERO   =                32768 / c
BSCALE  =                    1 / d
LOSTEVT =                    0 / T
SEED    =           1505889391 / S
THETA   =                60.83 / T
PHI     =                67.57 / P
ENERGY  =                 100. / E
END
```

Figure 4.6: *Left* : Header of output before modification. *Right* : Header of output after modification.

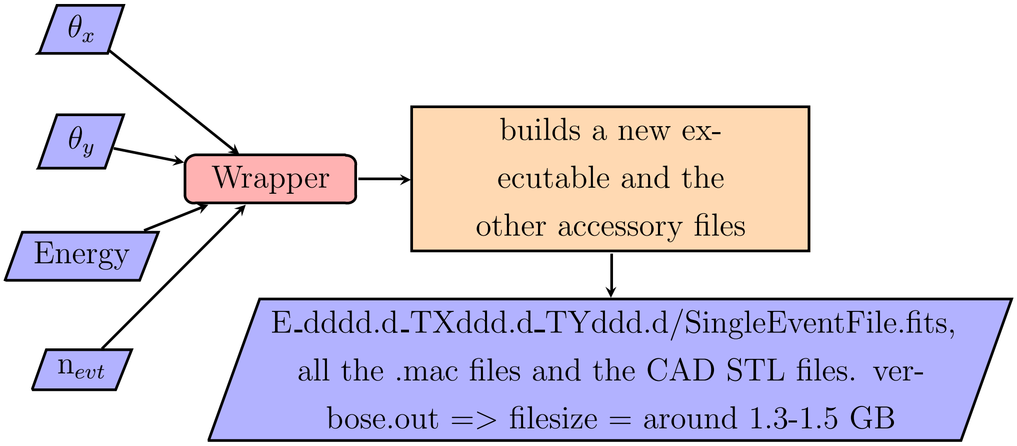

Figure 4.7: A flowchart of the process followed to run a simulation before modification.

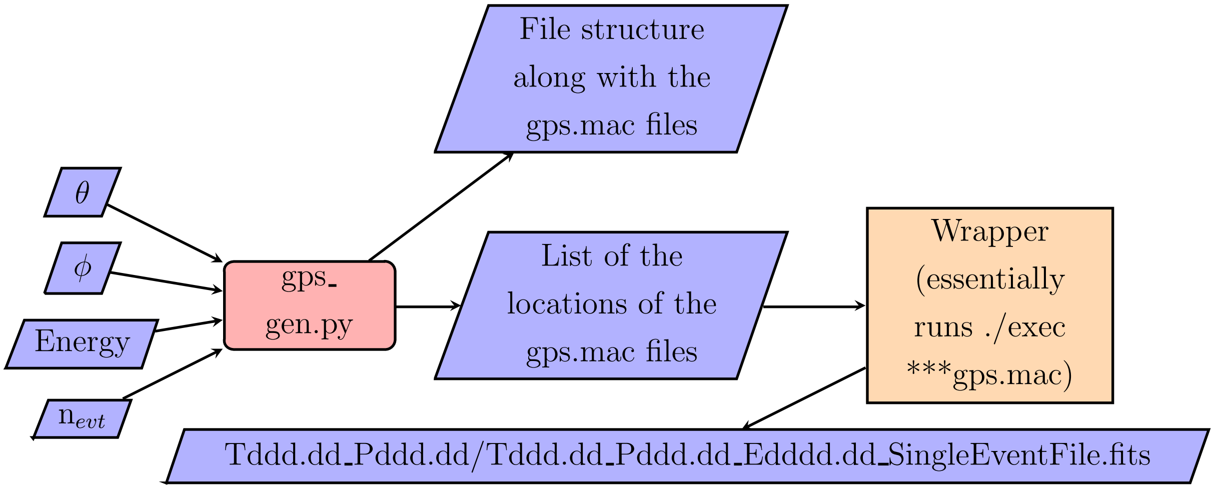

Figure 4.8: A flowchart of the process followed to run a simulation after modifications.

Figure 4.7, is a flow chart describing the procedure followed before the modifications, where θ_x and θ_y, the direction of incidence of the photons (refer 3.5), energy of the incident photons and n_{evt}, the number of incident photons are taken as inputs by a wrapper code that generates a gps macro file, with the input information for the mass model executable to read, and builds the main executable of the mass model every single time along with all the accessory detector construction files and other macro files. Then, the executable is run to get the output fits file, `Edddd.dd_TXddd.dd_TYddd.dd_/SingleEventFile.fits`, where `d` refers to a digit and `dddd.d` refers to the precision to which the respective values are recorded.

The output fits file has no meta data in its header on the direction of the source or the energy of the incident photons. Notice that the file inside `E.d_TXddd.d_TYddd.d` directory is named `SingleEventFile.fits`, hence making it difficult to identify which simulation it corresponds to if things get mixed up in different directories. Also, there were other files like the geometry CAD STL files, always copied into the output directory which made the size very large, to the order of 1.5 GB.

After modifications (Figure 4.8), the executable is built only once in the beginning during the installation of GEANT4. The inputs to the wrapper, `gps_gen.py` written by me, are θ, ϕ, energy of the incident photons and the number of photons, n_{evt}, illuminating the satellite. We have switched to the $\theta - \phi$ system as we have already seen that it is more easy to visualise mentally (refer Chapter 3.1.1). The wrapper generates the the gps macro file (already introduced in Figure 4.7) placed in a cleaner directory structure and a text file with the list of locations of the gps macro files. This list is given as input to another wrapper (written by Ajay Vibhute, IUCAA), which schedules the jobs to the cores of the cluster efficiently and executes the executable with the gps macro file already created by `gps_gen.py`. The final products for all different energies for a given direction of incidence are written into the already created directories, `Tddd.dd_Pddd.dd/`, with the file name, `Tddd.dd_Pddd.dd_Edddd.dd_SingleEventFile.fits`. The final file size has reduced drastically, with each output utilising about 16 MB in contrast to the 1.5 GB for each output before the modifications, allowing more storage for many more products.

Chapter 5

Testing and results

Equipped with all the information on transients, the instruments and the working of the codes let us look at some methods and results obtained during this thesis.

5.1 Gravitational wave counterpart search : Methods

The search for a counterpart to a gravitational wave starts with a trigger alert sent by LIGO consortium to the individuals/groups inside a Memorandum of Understanding (MoU) bracket. The alert contains the time of the trigger accompanied by a localisation map. Then a series of codes have to be run to check the detection status of CZTI. The codes for the analysis were already written before the commencing of this thesis and I learnt the working and ran them on a few triggers. Here, the process of the search is described using the example of the G298048, the trigger name given to GW170817 (details in the following section).

Once the trigger time is known, the archived CZTI data for that orbit of the satellite can be obtained from the servers in IUCAA, Pune. The raw data has to go through a series pipeline codes which gives out the cleaned data, making it suitable for more analysis. Next, histograms of the counts are plotted as function of time, called the **lightcurves** and also as function of energy for different time bins. This step provides a way to visually look at data and check for any patterns consistent with any counterparts that have been detected. The initial localisation map for this trigger is shown in Figure 5.1. All maps shown in this section are Mollweide projection maps.

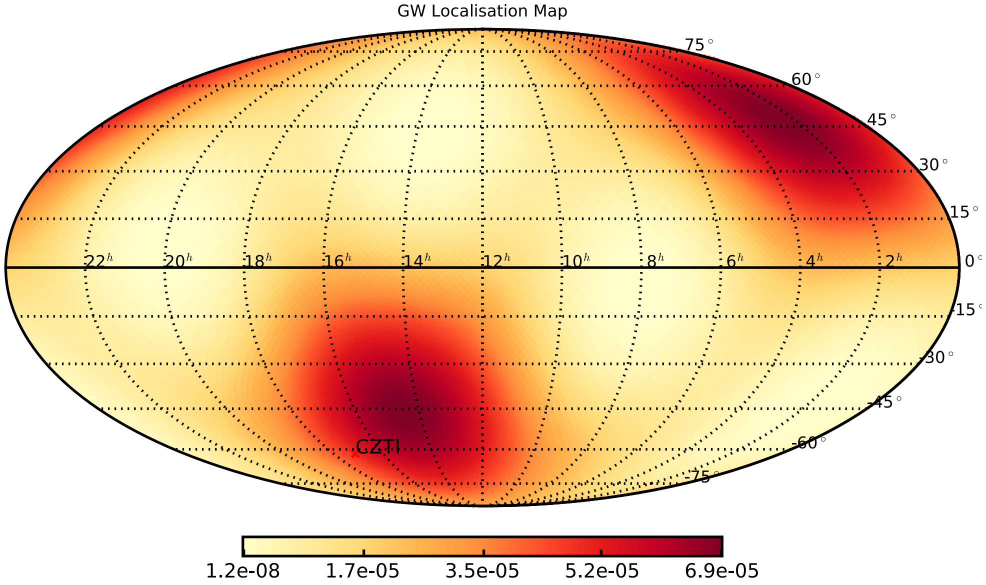

Figure 5.1: The initial localisation map for G298048 given by LIGO. The "CZTI" mark indicates the CZTI pointing direction (z-axis of CZTI).

The next step is to check what probability of the LIGO localisation region was visible to CZTI at the time of the trigger (see Figure 5.3). This is essential because the low earth orbit of AstroSat implies that about one third of the sky is occulted by the earth (see Figure 5.2). The yellow patch is the region of the sky visible to CZTI. The patch "Earth" is the part of the sky occulted by the earth. The patch "Behind" is the part of the sky below the plane of the detector.

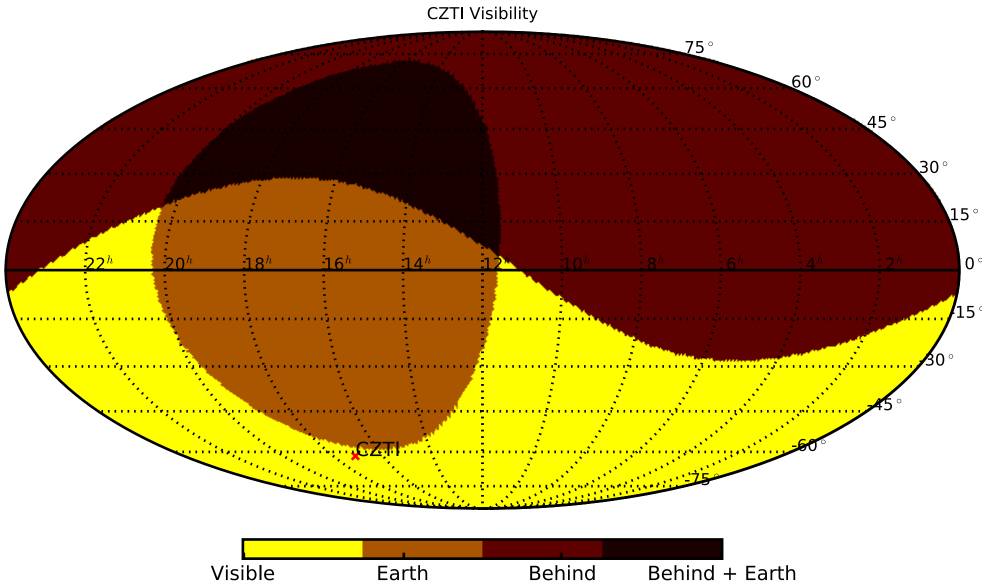

Figure 5.2: Sky visibility for CZTI at the trigger time of G298048. The "CZTI" mark indicates the CZTI pointing direction (z-axis of CZTI).

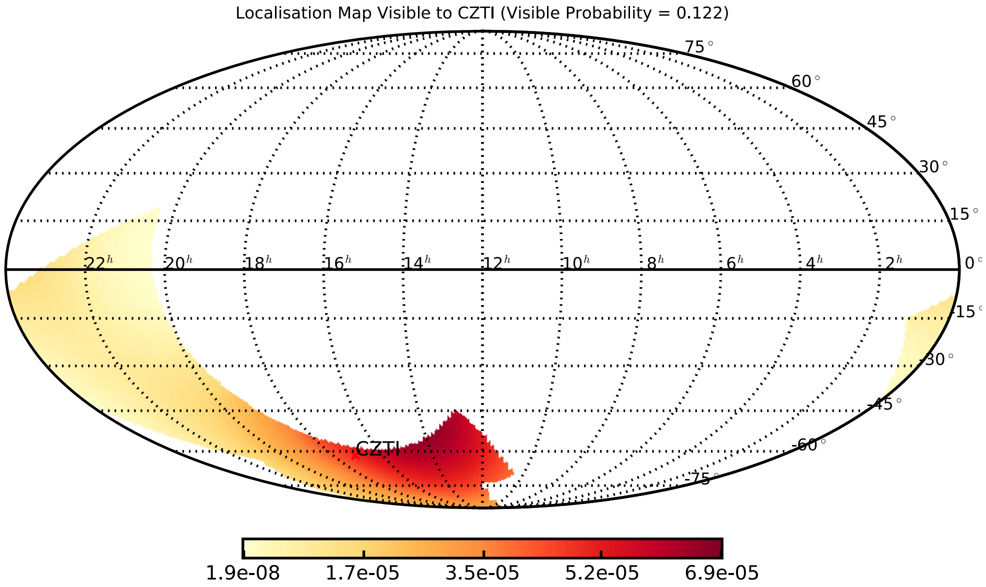

Figure 5.3: The probability of the LIGO localisation region for G298048 visible to CZTI. The "CZTI" mark indicates the CZTI pointing direction (z-axis of CZTI).

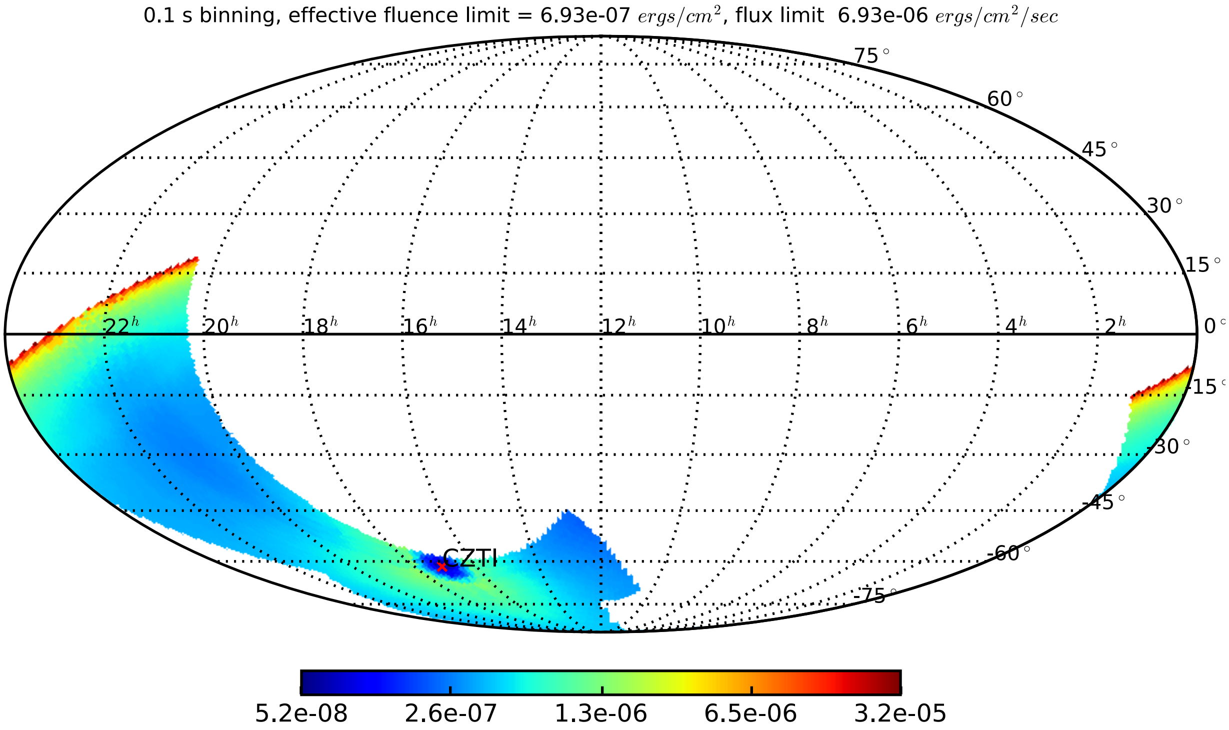

Figure 5.4: The CZTI upper limits for G298048 at 0.1 s binning. The "CZTI" mark indicates the CZTI pointing direction (z-axis of CZTI).

Upper limits are ideal estimates of fluxes assuming that the entire effective area, at the relevant direction and energy of photons, is illuminated equally. A set of codes estimate the minimum detectable photons per second, hereafter referred to as cutoff rates, for that particular orbit after analysing a few nearby orbits before and after the one of interest, and then finally calculate the upper limits for the flux and fluence values for different time bins, using effective areas calculated using raytrace simulation in the directions of the localisation region. The raytrace products were used during this analysis as the mass model was not fully developed during this analysis and that is the region for checking if the the source is above the plane of the detector in Figure 5.2. The upper limits from many instruments are published in non-refreed circulars known as Gamma-ray Coordination Network (GCN), maintained by National Aeronautics and Space Administration (NASA). [1]

---

[1] For more information refer to `https://gcn.gsfc.nasa.gov/`.

5.2 GW170817 : upper limits and localisation

G170817 is the first binary neutron star merger observed by the LIGO and VIRGO detectors and the first detected gravitational wave event accompanied by electromagnetic radiation. This event has erected a new milestone in electromagnetic follow-up of gravitational wave events with a huge number of observatories around the world contributing to the effort [13]. Here, our contribution to this effort will be discussed.

As soon as LIGO sent out its localisation map, we began scouring CZTI data and were unable to find anything in the data. Upper limits from CZTI for the GW170817 trigger as published in [3] (assuming band parameters $\alpha = -1.0$, $\beta = -2.5$ and $E_0 = 300$ keV) are tabulated below:

Table 5.1: CZTI upper limits for G298048

Time scales (s)	Fluence limit (ergs cm^{-2})	Flux limit (ergs cm^{-2} s^{-1})
0.1	6.93×10^{-7}	6.93×10^{-6}
1.0	1.65×10^{-6}	1.65×10^{-6}
10.0	2.05×10^{-6}	2.05×10^{-7}

Since AstroSat is a low earth orbit satellite (average height $\sim$ 650 km from earth surface), close to a third of the sky is always occulted by the earth. On closer look at the data we guessed that the source was behind the earth at the time of the the trigger. To confirm this, we ran a set of ray-trace simulations with the following powerlaw parameters for the GRB (obtained from Goldstein A. et al. 2017 [10]):

$$\begin{aligned} \alpha &= -0.88 \pm 0.44 \\ E_0 &= 128.0 \pm 48.7 \text{ keV} \\ fluence &= 2.2 \times 10^{-7} \text{erg cm}^{-2} \\ \text{location} : \theta_x &= 51^o, \theta_y = -33^o \end{aligned} \tag{5.1}$$

Since the source is shining from the open side of CZTI (not blocked by other satellite elements), changing the location slightly will not affect the effective area of the satellite much, resulting in similar counts registered. The powerlaw photon number flux is given by :

$$N(E) = AE^{\alpha}e^{\frac{-E}{E_0}} \tag{5.2}$$

It was assumed that α and E_0 are uncorrelated.

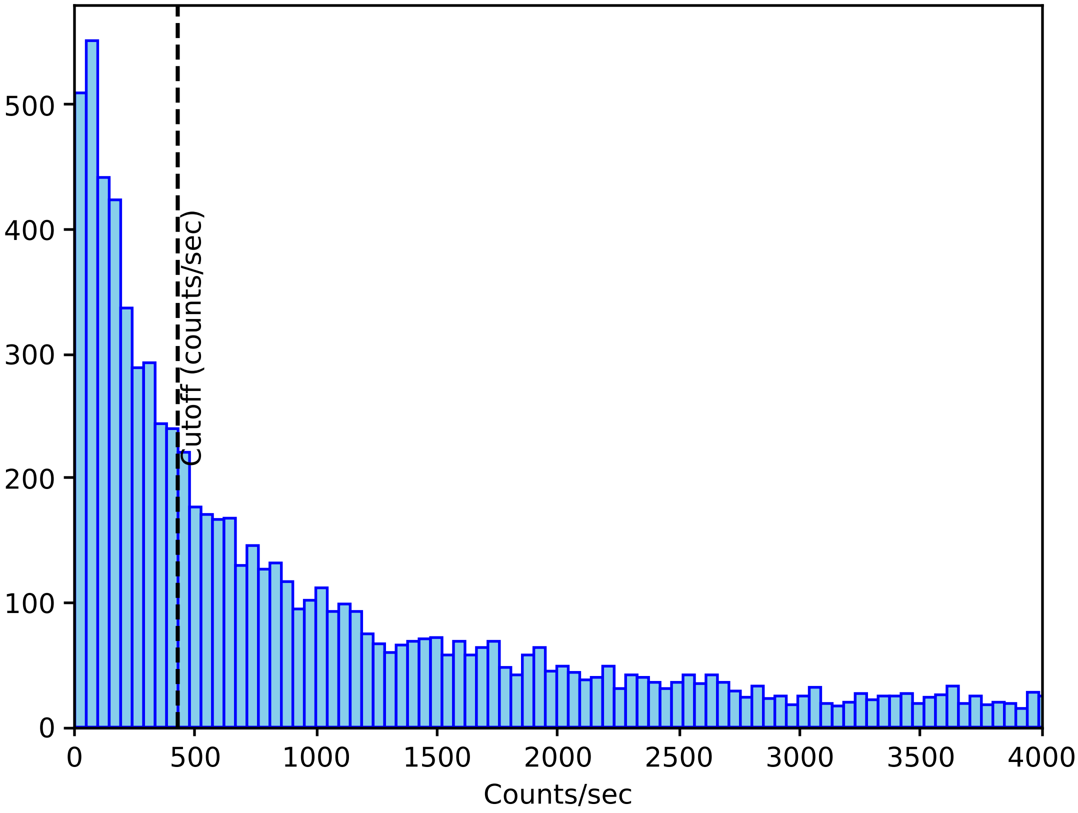

Figure 5.5: Histogram of total counts in 10000 simulations. We see that $\sim$ 66% of the simulations predict higher counts than the detection threshold (marked with the dotted line)

We see in Figure 5.5 that, for $\sim$ 66% of the simulations, the total counts/sec registered by CZTI is greater than the total cutoff counts (threshold counts/sec below which no detection is possible). The probability of non-detection is simply :

$$P(\text{non-detection}) = 100 - P(\text{detection})100 - 66 = 34\%$$

Of this 34%, there can be two possibilities: one, that the source is too faint and not occulted by earth and two, the source is too faint and behind the earth. The second term above will just be the fraction of the Fermi-GBM localisation (Figure6) region behind the earth($\sim \frac{1}{3}$), times the probability of non-detection (ie. $\sim \frac{1}{3}34 = 11.33\%$). Therefore the total probability of the source being behind earth is:

$$P(\text{source behind earth}) \approx 66 + 11.33 \approx 77\% \tag{5.3}$$

With this probability, the localisation of the source was improved (Figure 5.6). This result was published [11].

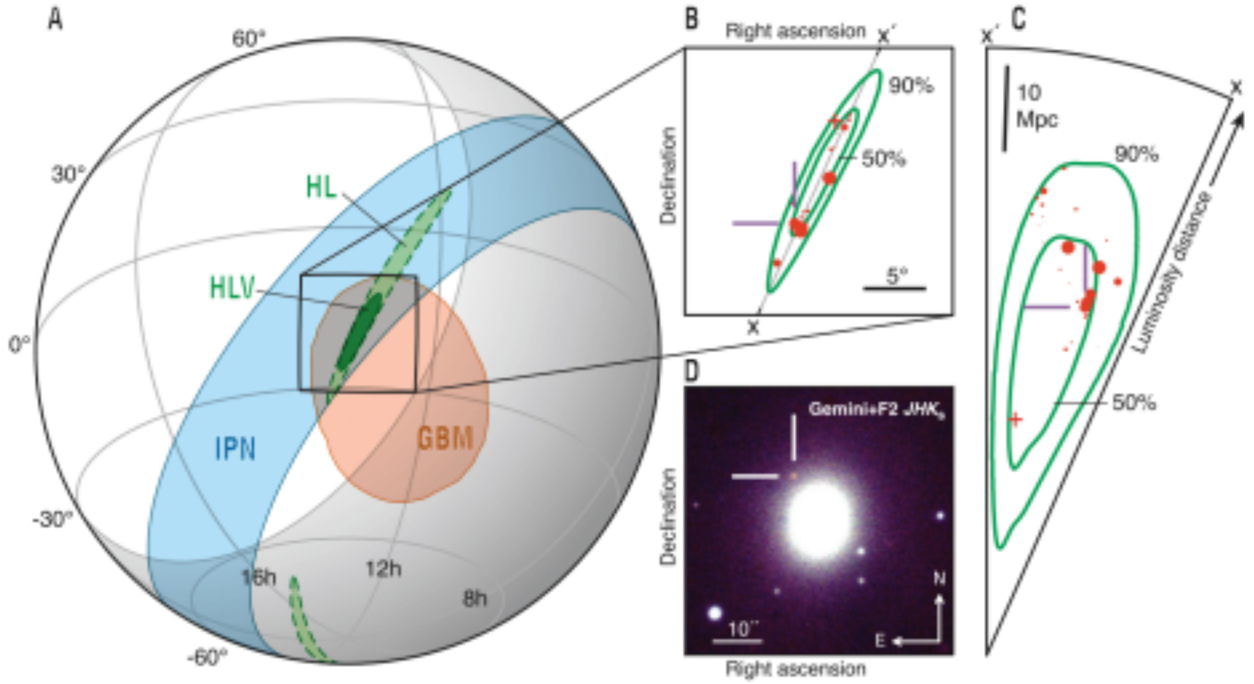

Figure 5.6: Localisation of the G170817 source. The white circle is the earth as seen by CZTI at the time of the trigger. See that it intersects the Fermi, LIGO, IPN localisations and the optical source was later identified in the intersection (inset). Figure taken from [11].

5.3 Method for localising GRBs using mass model

Detector Plane Histograms (DPHs) are a snapshot of the number of photons detected by each detector module (refer Figure 3.4 for the definition of a module) during the time of the trigger. Below, is an example of such a DPH with two different binnings. The DPH on the left is binned pixel-wise and it is seen that many pixels detect no counts. This is expected as we receive very few photons from a source. The module-wise binning (right) is a more robust one in which finding patterns is also possible. So, it was decided that we use this binning for all computations done, which require pattern comparisons.

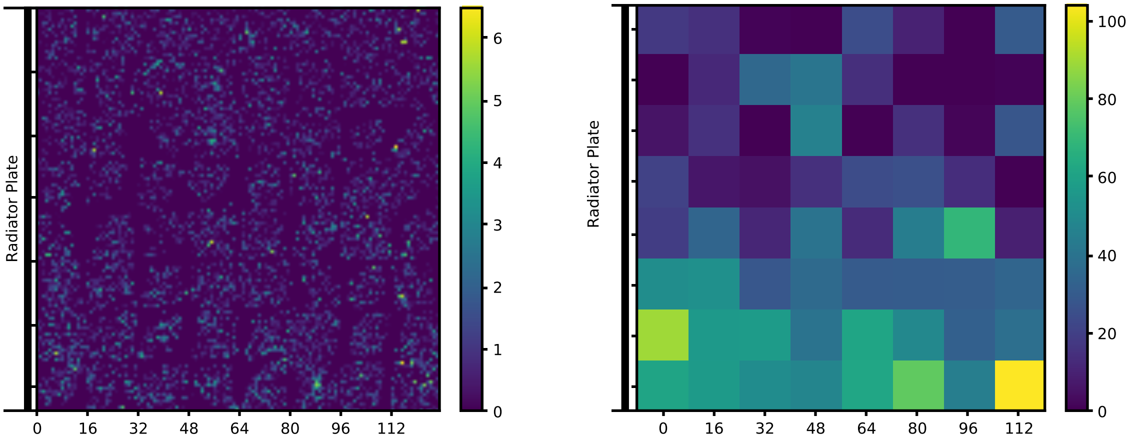

Figure 5.7: Example of the same DPH binned in two different ways. *Left* : Pixel-wise binning. *Right* : Module-wise binning.

The simulation products for different incident photon energies are stored in separate files (refer Chapter 4.2.1). Each of these files were created assuming a constant number of photons incident on the satellite. So, just adding the different energy files will not result in the desired simulated DPH. Hence, the counts are scaled by the Band law (refer Chapter 2.1) to simulate a source with known Band parameters. The observed DPH is prepared by subtracting background from the trigger region of the lightcurve (refer Chapter 2.1).

Having obtained the observed DPH, a series of simulated DPHs are made from a grid of mass model products (Chapter 5.4) and compared with the observed DPH using χ^2 **test for goodness of fit**.

5.3.1 χ^2 test for goodness of fit [5]

χ^2 is a good statistic to measure the deviation of data from a model and to validate the correctness of a model. For our case, the value of χ^2 can be calculated as follows :

$$\chi^2 = \sum \frac{(\mathrm{C_{sim}} - \mathrm{C_{obs}})^2}{(\mathrm{Err}^2_{\mathrm{sim}} + \mathrm{Err}^2_{\mathrm{obs}})} \tag{5.4}$$

where $\mathrm{C_{sim}}$ and $\mathrm{C_{obs}}$ are the simulated counts and observed counts in that module and $\mathrm{Err_{sim}}$ and $\mathrm{Err_{obs}}$ are their corresponding errors. The probability distribution function (P) for χ^2 distribution for ν degrees of freedom is given by :

$$P(x,\nu) = \frac{x^{\frac{\nu}{2}-1} e^{\frac{-x}{2}}}{2^{\frac{\nu}{2}} \Gamma(\frac{\nu}{2})} \quad ; \quad x > 0 \tag{5.5}$$

where, $\Gamma(n+1) = n!$ for integer n. The minimum value of χ^2 for a comparison with degree of freedom, ν, is ν. A fit is "good", if the value of the χ^2 obtained is minimum and ideally close to the number of degrees of freedom of the problem. In reality the minimum of the χ^2 surface (χ^2, in our problem is a function of two coordinates on the sky. Hence, surface.) is not ν and therefore, all χ^2 values are scaled such that the minimum of the χ^2 surface equals ν.

This statistic will be used to compare an observed DPH against a grid of expected DPHs to obtain confidence contours for the locating the source on the sky (refer Chapter 5.6).

5.4 Mass model grid

After establishing the statistical methods, we have seen that we need to compare the observed DPHs with simulated DPHs from different regions of the sky as seen from the instrument. What we need, is a grid of simulated products distributed uniformly all over the sky. The following sub-section describes the method used for pixelating the sky.

5.4.1 Hierarchical Triangular Mesh (HTM)

The simulation grid should be uniform all over the sky and using a uniformly spaced grid in θ and ϕ is **not** the solution (the points will cluster near the poles, ie $\theta \to 0$ or 180). In other words, we need to pixelate the sky such that all pixels have equal area. Hierarchical Triangular Mesh (HTM) is a method which involves dividing a sphere into spherical triangular pixels, *trixels*, of equal areas [16]. Such a division can be done in many levels depending on the resolution of the grid (the area of each trixel). All coordinates are given in the $\theta - \phi$ system from here on. The smallest possible division (*level 0*) consists of 8 trixels and is shown below :

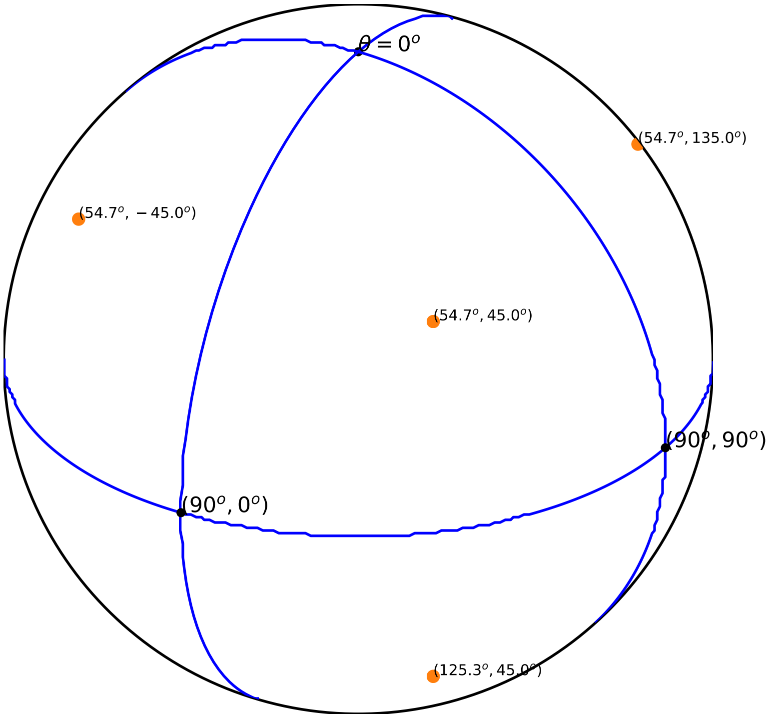

Figure 5.8: Level 0 HTM grid. The sphere is divided into octants and 8 trixels are obtained and the centers of the trixels are marked orange.

The subsequent levels can be obtained recursively by joining the centers of the sides of the triangular pixels using **great circles** (circles on the sphere obtained at the intersection of a plane passing through the two points of interest and the center of the sphere with the sphere itself).

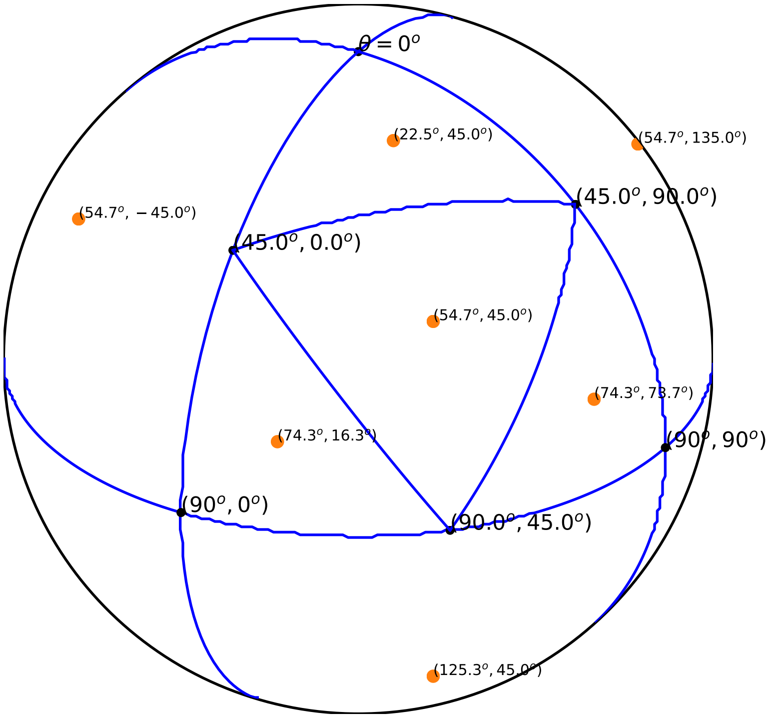

Figure 5.9: An illustration on how to obtain the grid for the next level (level 1, in this case). Here, I have done the division for only one of the bigger level 0 trixels (refer Figure 5.8). Notice that the center of the level 0 trixel is also the center of the new central level 1 trixel. The centers of the trixels are marked orange.

The advantage of HTM over other methods of equal area pixelation of the sky like Healpix [2], is evident from Figure 5.9. We see that the central trixel has the same coordinates as the level 0 trixel. Therefore, to make finer grids, we only need to run the simulations for the new three locations per coarse trixel, instead of running the simulations for entirely new set of points.

We now have a level 4 grid (refer Figure 5.10), constructed from the mass model products for localising sources. The grid points were calculated using the python package, `esutil` [3].

---

[2] refer to https://healpix.jpl.nasa.gov/

[3] https://github.com/esheldon/esutil

The developer of this package was very helpful in implementing certain methods that were required for calculation of the grid points. This simulation grid was run in the Physical Research Laboratory cluster by Aarthy E. and took around 30 days to complete.

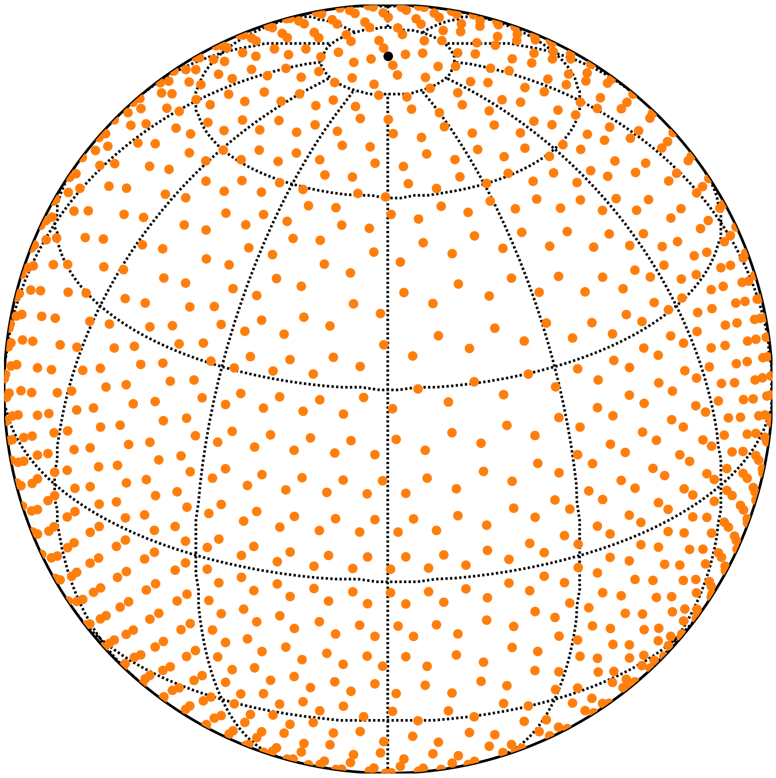

Figure 5.10: Level 4 HTM mass model grid. The orange points are the pixel centers

5.5 All sky sensitivity

Effective area, as a measure on sensitivity has already been introduced in Chapter 4. Presented below, are plots of the effective area as a function of direction of incidence of photons for two different incident photon energies. The orientation of the coordinate axes for this is mentioned in the caption. The plots on the left panel are obtained from the raytrace grid, already discussed in Chapter 4.1. The plots on the right are from the mass model grid (refer previous section). Here we obtain the effective area for all the regions of the sky.

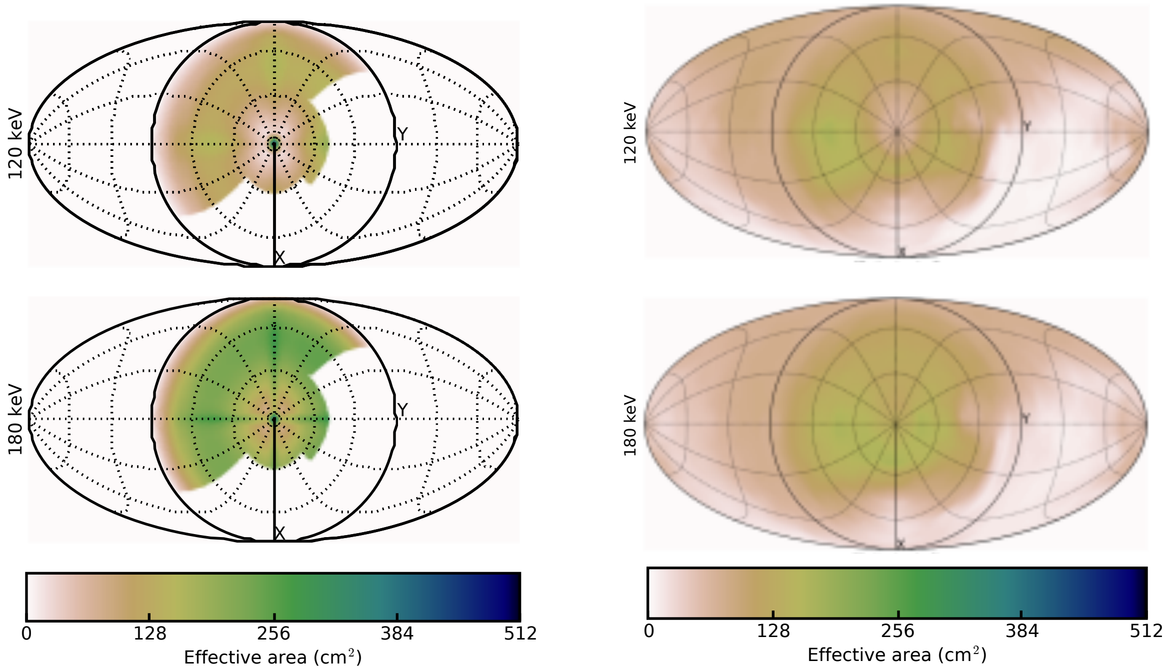

Figure 5.11: Mollweide projection plots of the whole sky as seen by CZTI. The z-axis of CZTI points out of the paper, the x-axis points down and the y-axis points to the right. *Left* : The effective area calculated using Raytrace simulations (discussed in Chapter 4.1). Figure from [6]. *Right* : Effective areas at the same incident photon energies using mass model products.

5.6 Localising an artificially injected GRB

Let us inject an artificial GRB, by taking a simulated DPH from the grid and add Poisson noise and residual background to mimic a real GRB, with the following parameters :

$$\text{Coordinates : } \theta = 39.16^o, \phi = 153.40^o$$

$$\text{Band Parameters : } \alpha = -1.0, \beta = -2.5, E_{\text{peak}} = 300 \text{ keV}, Norm = 1.035$$

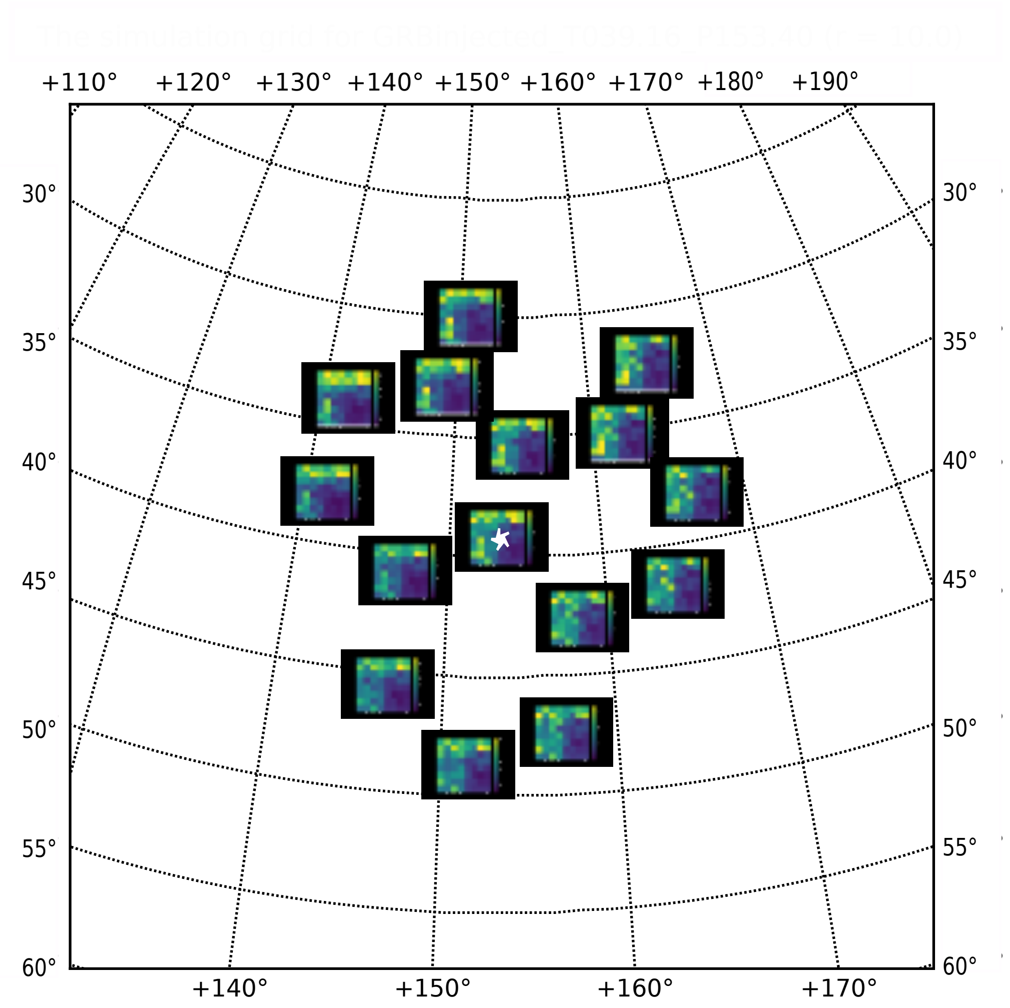

Figure 5.12: The simulated DPHs at the selected grid points over-plotted on the grid of points over which the comparison is to be done. Here, we know the rough location of the GRB (marked with the white star in the center) already, so we need not do the comparison for the whole sky. Notice the change in the pattern of the DPH with change in direction of incidence.

The plot above shows the the simulated DPHs at all the grid points that have chosen for the χ^2 test. We need not run the comparison for points all over the sky as we already have a rough location of the source. In cases where we don't have a rough location, the following analysis must be done with the whole sky grid.

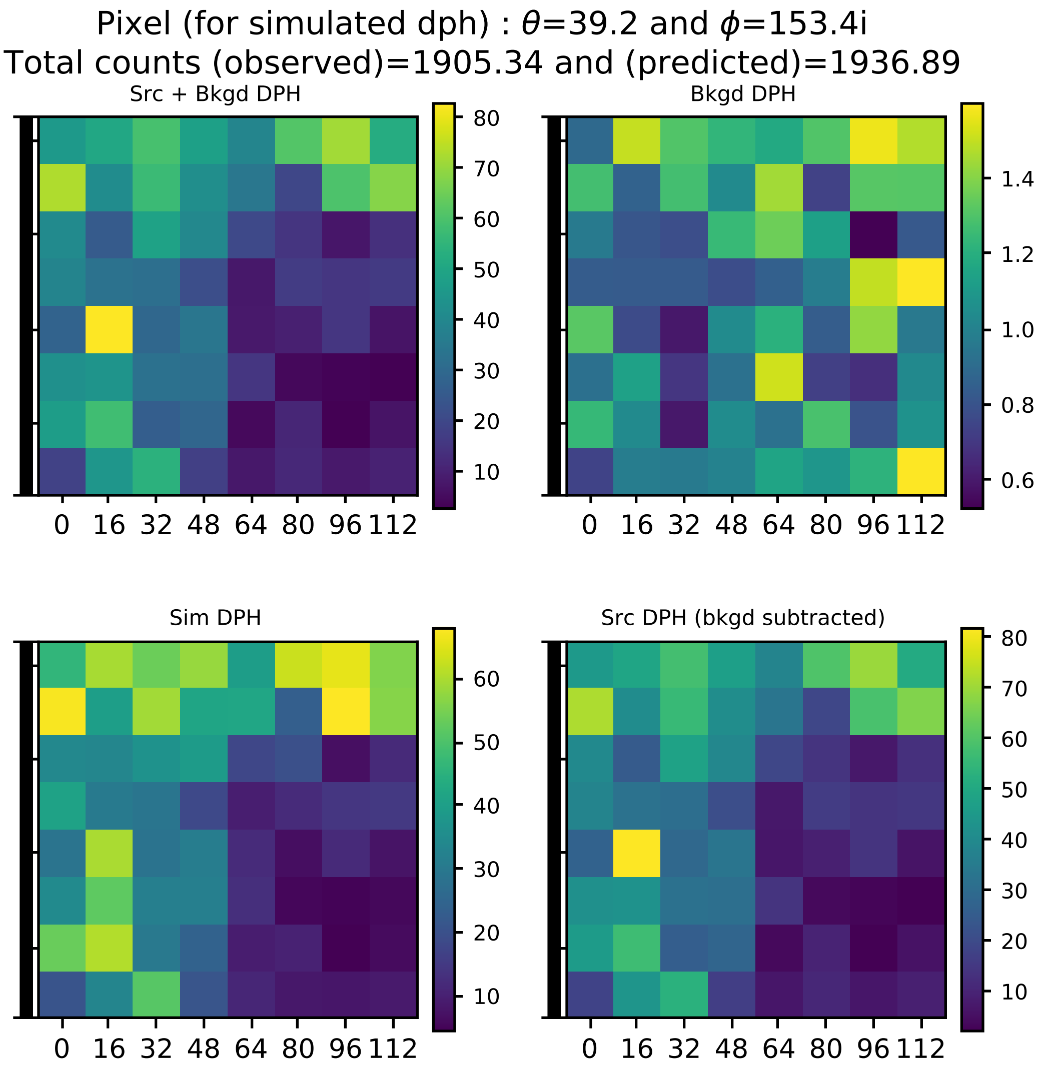

Figure 5.13: This plot shows the various DPHs that are calculated. The two DPHs on the bottom are the ones that are compared using the χ^2 analysis.

Now, at the location of the GRB, a plot of all the relevant DPHs are made as shown above. The same comparison is done for all the points on the above sub-grid, but the following plot is only made for the simulated point closest to the known GRB location.

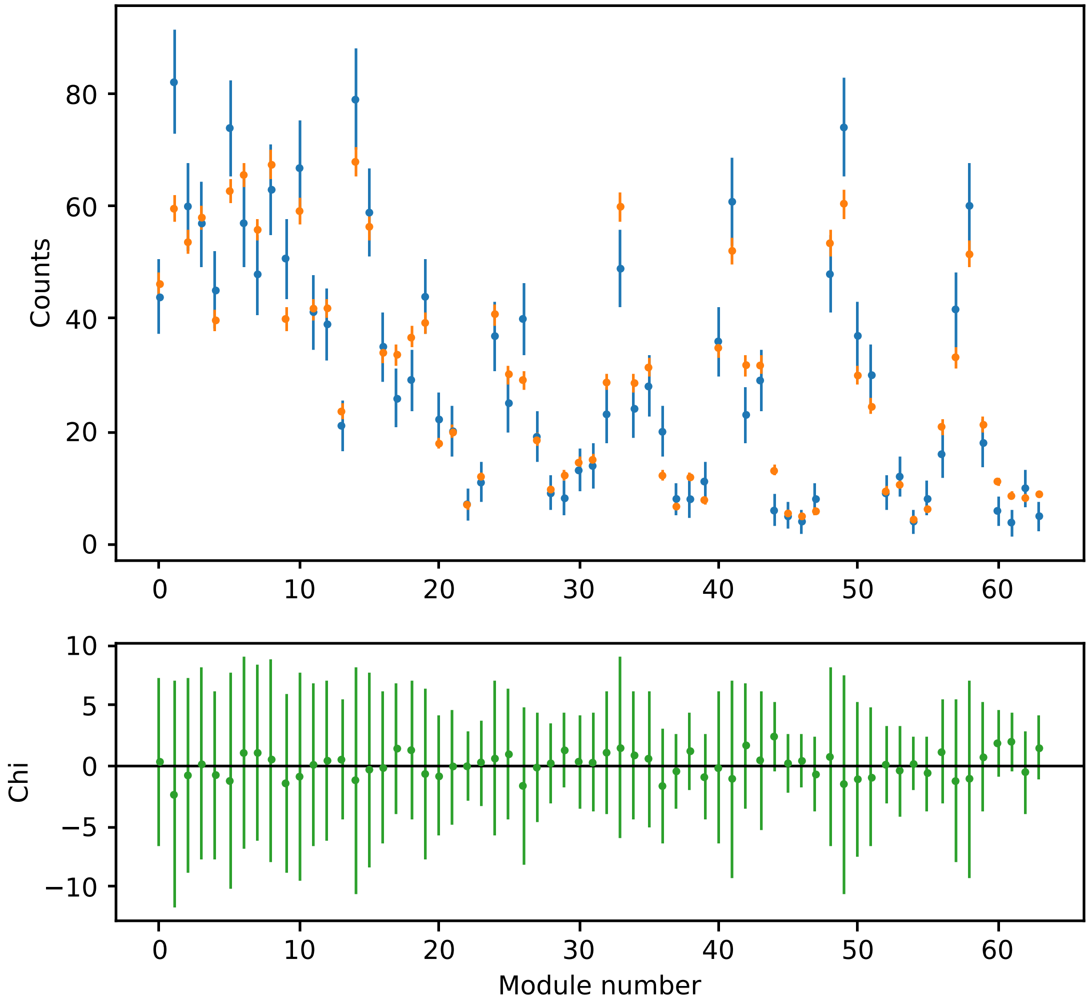

Figure 5.14: A plot of the observed and simulated counts (module wise). The bottom panel is a plot of the $\sqrt{\chi^2}$ at every point. It is a measure of deviation (from "0 χ" marked in the graph) of model (simulation) from data (observation).

In the graph above, the top panel shows the counts detected in each module over-plotted with those expected in that module along with their corresponding errors. The lower panel plots the $\sqrt{\chi^2}$ for every module. It is a measure of the deviation of the observed data from the expected values.

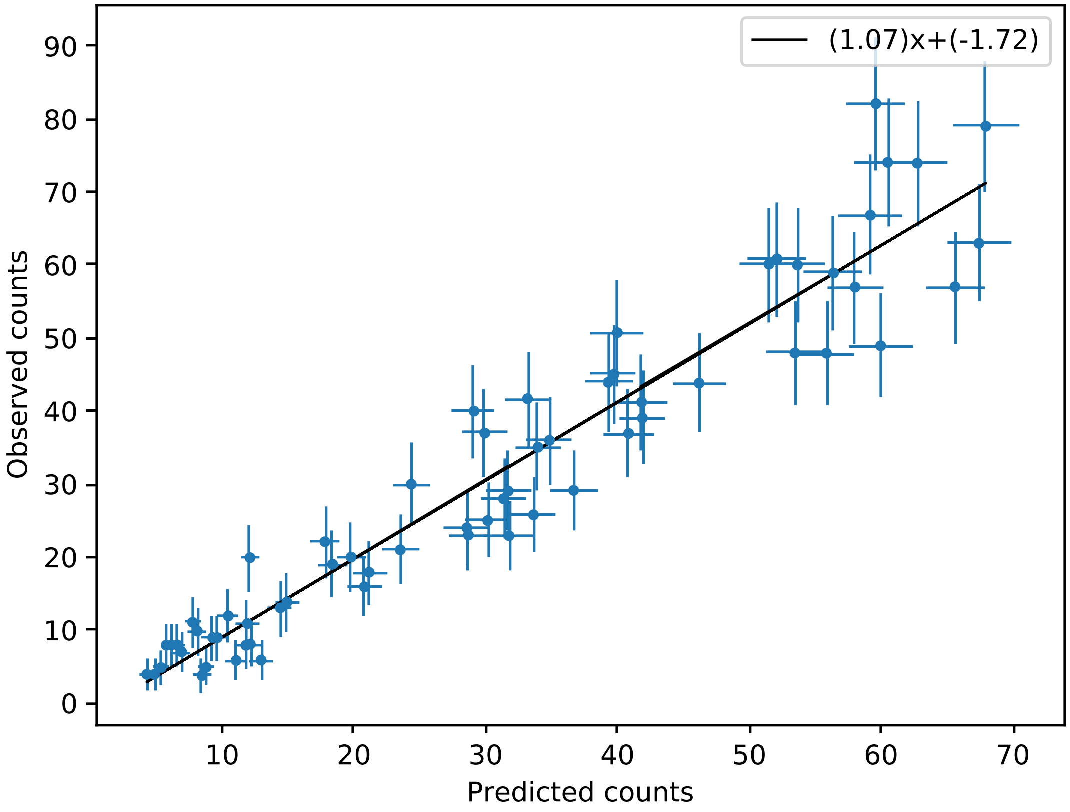

Figure 5.15: A plot showing observed counts as a function of predicted counts with a straight line fit. Sometimes, the spectral parameters known for the GRB might be uncertain. Therefore, the model can be scaled linearly with an intercept, and the χ^2 comparison repeated.

Here, we fit a straight line to the observed vs predicted counts graph and scale the predicted counts by the parameters of the line obtained as the calculation of norm, A, of the band spectrum may not be right when we are assuming parameters from some other satellite. Also, if there is a trend in the lightcurve of the GRB, there might be a constant shift in the observed counts, which are not considered while doing the simulation. So, we finally get :

$$\text{Scaled expected counts} = \text{slope} \times (\text{expected counts}) + (\text{intercept})$$

The χ^2 comparison is carried out for both the pairs : observed and unscaled predicted DPHs and also for the observed and scaled predicted DPHs (refer Figure 5.16). For the χ^2 comparison between the observed and unscaled predicted DPHs, the degrees of freedom, ν, will be 62 (64 modules with two free parameters - θ and ϕ) and for that for the observed and scaled predicted DPHs will be 60 (64 modules with four free parameters - θ, ϕ, slope of the fit, intercept of the fit).

Confidence contour levels (for the ideal case where the minimum of the χ^2 surface is equal to number of degrees of freedom) that were selected to be drawn are tabulated below :

Table 5.2: χ^2 confidence levels

contour level	dof	1-σ	2-σ	3-σ	90%	99%
unscaled predictions	62	63	64	65	76.6	90.8
scaled predictions	60	61	62	63	74.4	88.4

where, $n - \sigma$ contour is just $(\min(\chi^2) + n)$ and the 90% and 99% contours can be looked up from standard χ^2 tables [4]. As already discussed above, in reality, the minimum of the χ^2 surface may not equal the number of degrees of freedom. In that case, all the above levels are scaled appropriately. For instance, if the minimum χ^2 for the unscaled comparison is 63, then the 1-σ contour level will be $63 + 1 \times \frac{63}{62} = 64.016$, instead of 63.

---

[4] `https://www.medcalc.org/manual/chi-square-table.php`

With all the information gathered from above calculations, we can proceed to plotting the contour levels. The top panel has the 1-σ, 2-σ and 3-σ contours for both the unscaled (left) and scaled (right) comparisons and the bottom panel contains the 90% and 99% contours.

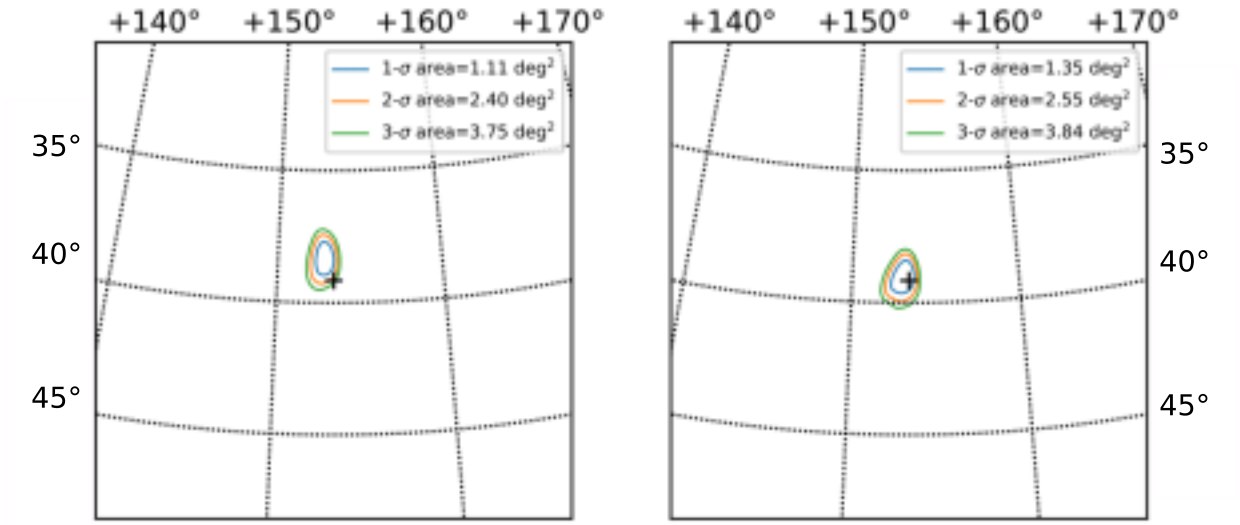

Unscaled comparison

Scaled comparison

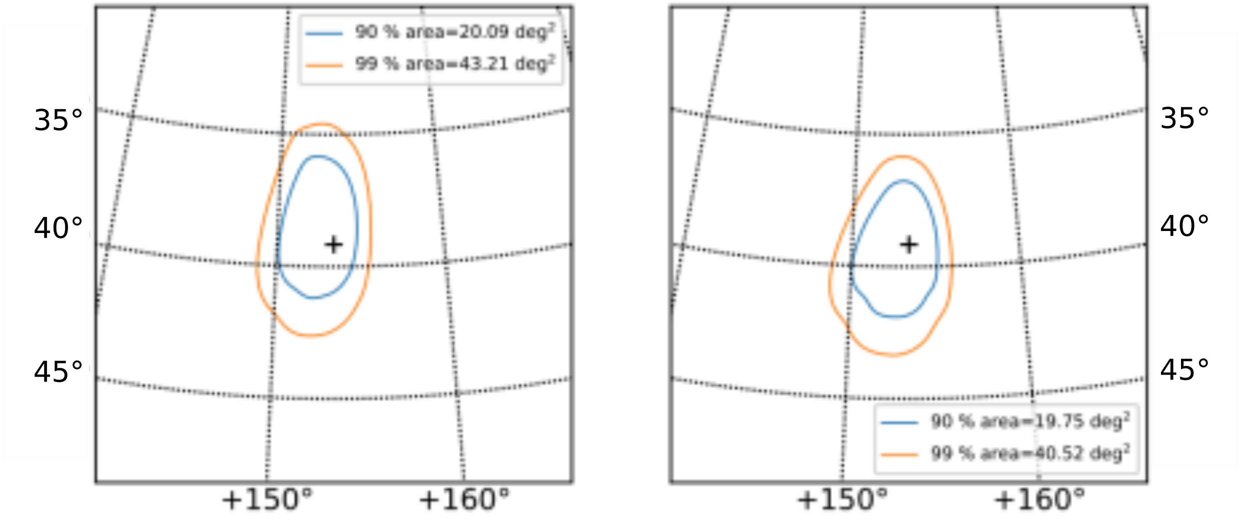

Figure 5.16: Plot showing all contour levels for this injected GRB. Panels on the left are for the unscaled predictions compared with the observations and panels on the right for the scaled predictions compared with the observations. The panels on the top show the $n - \sigma$ contours while the ones on the bottom show the 90% and the 99% contours. The areas of each contour is printed in the legend for each plot.

5.7 Localising a real GRB

Following the same process as the previous section, the localisation for GRB160802A has been shown below. The parameters for the GRB are (spectral parameters obtained from Fermi Burst Catalog [5]):

$$\text{Coordinates}: \theta = 53.0^o, \phi = 273.1^o$$

$$\text{Band Parameters}: \alpha = -0.7, \beta = -2.5, E_{\text{peak}} = 275 \text{ keV}, Norm = 0.03$$

The lightcurve, a plot of the counts as a function of time for the GRB is shown below along with the regions taken as **background**. X-rays from a constant source and other noise in the system cause the detector to always register some counts, known as background. These counts need to be subtracted from the trigger to get photons only from the source. So, choosing a region around the GRB and subtracting a properly scaled number of counts does the trick.

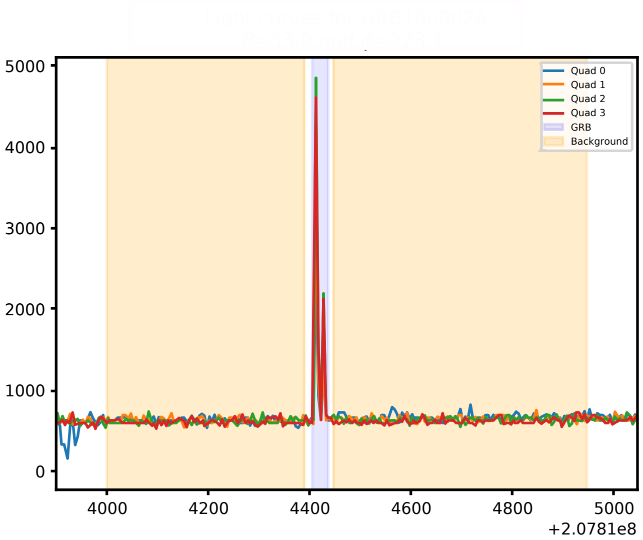

Figure 5.17: Plot showing lightcurves for all quadrants (refer Figure 3.4 for the quadrant naming convention) for GRB160802A at 5 s binning. The blue region is the GRB and the orange region is the background.

---

[5] https://heasarc.gsfc.nasa.gov/db-perl/W3Browse/w3query.pl

The following figure shows the source + background, the background, the simulated and the source - background DPHs for the GRB. The DPHs in the bottom panel are the ones considered for the comparison.

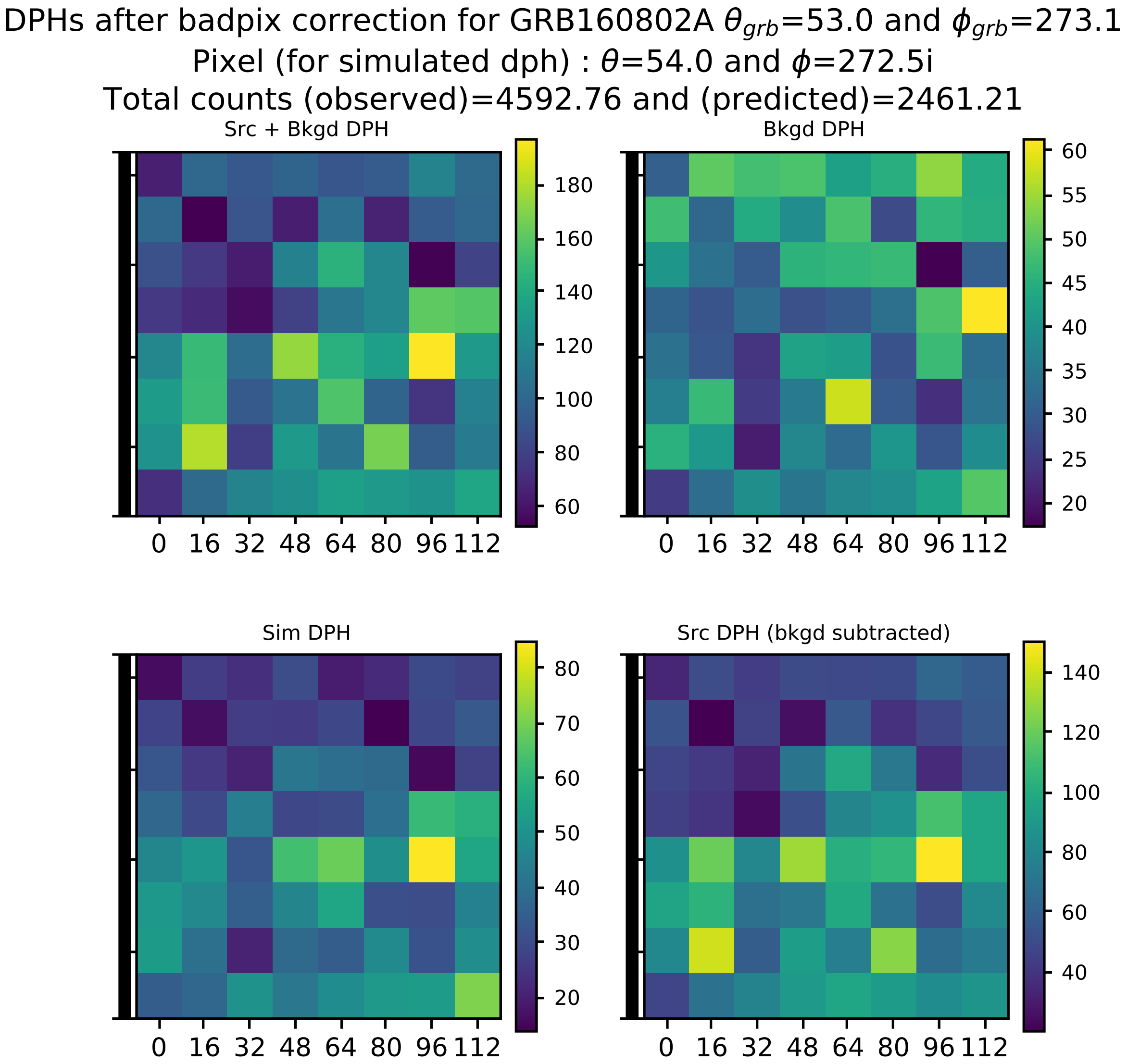

Figure 5.18: Plot showing the DPHs for GRB160802A.

Now, the χ^2 confidence contours are plotted in the same format as Figure 5.16

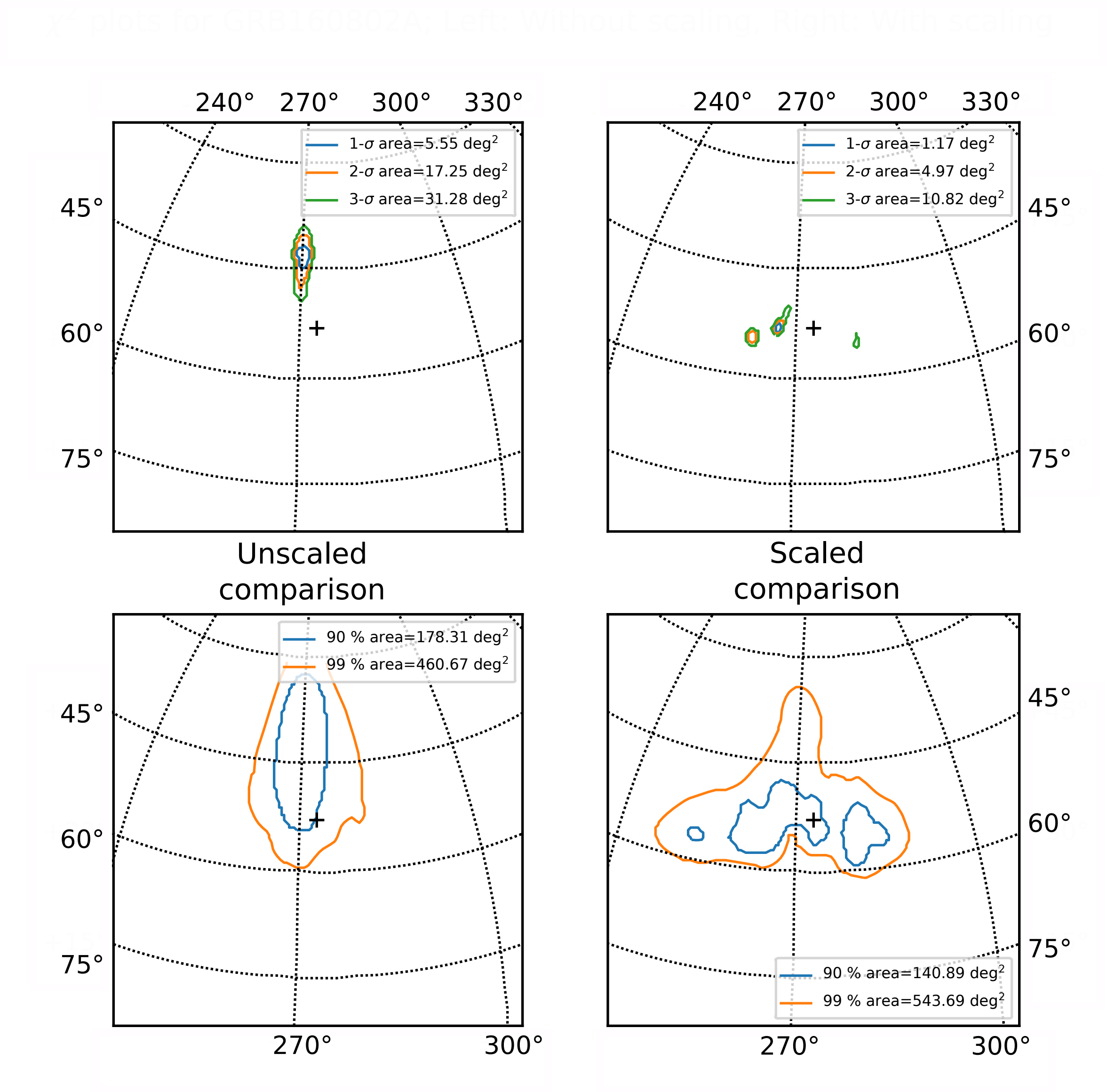

Figure 5.19: Plot showing the confidence contours for this GRB. The panels on the top show the $n-\sigma$ contours while the ones on the bottom show the 90% and the 99% contours. The areas of each contour is printed in the legend for each plot

Such analysis has been done for a set of bright GRBs that have been detected by CZTI. A publication is being prepared with the systematic study of localisation using mass model products.

Chapter 6

Conclusion and future work

The atmosphere of the earth blocks out X-ray radiation from outer space. We need to go beyond the atmosphere to study them. The detection mechanisms employed to study X-rays are quite different from other lower energy radiation. Transients are short timescale events which occur due to various mechanisms. GRBs and electromagnetic counterparts are transients that are relevant to this thesis. The satellite, our eyes on the sky, AstroSat, consists of a hard X-ray instrument, CZTI, which is the instrument used for obtaining data analysed and used during this thesis project. CZTI can be used as an off-axis GRB and electromagnetic counterpart detector due to the advantage of it being an open detector to photons above a hundred keV. We need simulations to understand the myriad photon interactions with other satellite elements before reaching the CZT detector. The mass model is an improvement from already existing raytrace simulations due to the modelling of all interactions and its all-sky coverage. The modifications made to the mass model during the thesis, helped making large scale runs possible and in better housekeeping of the output products. Using the tools developed, some results on the gravitational wave counterpart search, GW170817 event, localisation of GRBs, the development of the mass model all-sky grid and hence the all-sky sensitivity of the instrument have been possible.

Though considerable progress has been made in the study of transients using CZTI through the course of this thesis, a lot remains to be done. Future work will include :

- Improving the localisation of GRBs using given spectra for improved GW follow-up.
- Making a spectral response matrix that will help in fitting spectra to GRBs of known locations. This will involve solving the problem of a 60 keV tantalum fluorescence line that is seen in all spectra due to the presence of tantalum collimators above the detector.
- Independent localisation and spectra from CZTI itself.

Bibliography

[1] B. P. Abbott et al. “GW170817: Observation of Gravitational Waves from a Binary Neutron Star Inspiral”. In: *Physical Review Letters* 119.16 (2017), pp. 30–33. ISSN: 10797114. DOI: `10.1103/PhysRevLett.119.161101`. arXiv: `1710.05836`. URL: `https://journals.aps.org/prl/pdf/10.1103/PhysRevLett.119.161101`.

[2] B P Abbott et al. “Observation of gravitational waves from a binary black hole merger”. In: *Physical Review Letters* 116.6 (2016). ISSN: 10797114. DOI: `10.1103/PhysRevLett.116.061102`. arXiv: `1602.03837`. URL: `https://journals.aps.org/prl/pdf/10.1103/PhysRevLett.116.061102`.

[3] A. Balasubramanian et al. “LIGO/Virgo G298048: Astrosat CZTI upper limits”. In: *GRB Coordinates Network* 21514 (2017), p. 1.

[4] D. Band et al. “BATSE observations of gamma-ray burst spectra. I - Spectral diversity”. In: *The Astrophysical Journal* 413 (1993), p. 281. ISSN: 0004-637X. DOI: `10.1086/172995`. URL: `http://adsabs.harvard.edu/doi/10.1086/172995`.

[5] Philip Bevington R. and Keith Robinson D. *Data Reduction and Error Analysis for the Physical Sciences*. Third Edition 1992. ISBN: 0-07-247227-8.

[6] V. Bhalerao et al. “The Cadmium Zinc Telluride Imager on AstroSat”. In: *Journal of Astrophysics and Astronomy* 38.2 (2017). ISSN: 09737758. DOI: `10.1007/s12036-017-9447-8`. arXiv: `1608.03408`.

[7] E. Caroli et al. “Coded aperture imaging in X- and gamma-ray astronomy”. In: *Space Science Reviews* 45.3-4 (1987), pp. 349–403. ISSN: 00386308. DOI: `10.1007/BF00171998`.

[8] Bradley . W Carroll and Dale . a. Ostlie. *An introduction to modern astrophysics*. Vol. 44. 10. 2007, p. 1358. ISBN: 0-321-44264-9. DOI: `10.5860/CHOICE.44-5618`.

[9] Geant4 Community. *Introduction to Geant4 : Release Documentation*. Vol. 10.4. June. 2004, pp. 2–9. ISBN: 0805353402. URL: `http://geant4.web.cern.ch/geant4/support/ReleaseNotes4.10.4.html`.

[10] A. Goldstein et al. "LIGO/Virgo G298048 - Update on Fermi/GBM GRB 170817A Analysis". In: *GRB Coordinates Network* 21528 (2017), p. 1.

[11] M. M. Kasliwal et al. "Illuminating gravitational waves: A concordant picture of photons from a neutron star merger". In: *Science* 358.6370 (2017), pp. 1559–1565. ISSN: 10959203. DOI: `10.1126/science.aap9455`. arXiv: `1710.05436`.

[12] Glenn F. Knoll. *Radiation Detection and Measurement*. 2010, p. 860. ISBN: 0470131489. DOI: `10.1017/CBO9781107415324.004`. URL: `https://books.google.com/books?hl=en%7B%5C&%7Dlr=%7B%5C&%7Did=4vTJ7UDel5IC%7B%5C&%7Dpgis=1`.

[13] LIGO Scientific Collaboration et al. "Multi-messenger Observations of a Binary Neutron Star Merger". In: 12 (2017). ISSN: 2041-8205. DOI: `10.3847/2041-8213/aa91c9`. arXiv: `1710.05833`. URL: `http://arxiv.org/abs/1710.05833%7B%5C%%7D0Ahttp://dx.doi.org/10.3847/2041-8213/aa91c9`.

[14] B. D. Metzger and E. Berger. "What is the most promising electromagnetic counterpart of a neutron star binary merger?" In: *Astrophysical Journal* 746.1 (2012). ISSN: 15384357. DOI: `10.1088/0004-637X/746/1/48`. arXiv: `1108.6056`.

[15] K. P. Singh et al. "ASTROSAT mission". In: *Space Telescopes and Instrumentation 2014: Ultraviolet to Gamma Ray*. Vol. 9144. July 2014, 91441S. DOI: `10.1117/12.2062667`.

[16] Alexander S. Szalay et al. "Indexing the Sphere with the Hierarchical Triangular Mesh". In: (2007). arXiv: `0701164 [cs]`. URL: `http://arxiv.org/abs/cs/0701164`.

[17] Tadayuki Takahashi and Shin Watanabe. "Recent progress in CdTe and CdZnTe detectors". In: *IEEE Transactions on Nuclear Science* 48.4 I (2001), pp. 950–959. ISSN: 00189499. DOI: `10.1109/23.958705`. arXiv: `0107398 [astro-ph]`.

[18] D.C. Wells, E.W. Greisen, and R.H. Harten. "FITS: A flexible image transport system". In: *Astronomy & Astrophysics Supplement Series* 44 (1981), pp. 363–370. ISSN: 0365-0138.

[19] Bing Zhang. "Gamma-Ray Burst Prompt Emission". In: *International Journal of Modern Physics D* (2014). ISSN: 0218-2718. DOI: 10.1142/S021827181430002X. arXiv: 1402.7022. URL: https://arxiv.org/pdf/1402.7022.pdf%20http://arxiv.org/abs/1402.7022%7B%5C%%7D0Ahttp://dx.doi.org/10.1142/S021827181430002X.